Ultra-Lightweight High-Efficiency Buck-Boost DC-DC Converters for Future eVTOL Aircraft with Hybrid Power Supply

D. Menzi,
L. Imperiali,
E. Bürgisser,
M. Ulmer,
J. Huber,
J. W. Kolar

Ultra-Lightweight High-Efficiency Buck-Boost DC-DC Converters for Future eVTOL Aircraft with Hybrid Power Supply

David Menzi, *Member, IEEE,* Luc Imperiali, *Student Member, IEEE,* Elias Bürgisser, Martin Ulmer, Jonas Huber, *Senior Member, IEEE,* Johann W. Kolar, *Fellow, IEEE*

Abstract—The trend towards urbanization intensifies road congestion and thus increases interest in research on urban air mobility. Electric motors enable lightweight distributed propulsion in all-electric vertical take-off and landing (eVTOL) aircraft which combine the advantages of helicopters (low operating space requirement for take-off and landing) and fixed-wing planes (efficient cruising). When aiming at ranges beyond 300 km, a hybrid power supply architecture leveraging the advantages of Fuel-Cells (FCs; with high gravimetric energy density) and batteries (with high gravimetric power density) is required, as weight is a key performance metric in airborne applications. To regulate the power flow between the two energy sources with their respective dc terminal voltages varying in a wide range, a Buck-Boost (BB) dc-dc converter is required. Such BB dc-dc converters are, however, understudied in literature and gravimetric power densities today are limited to 20 kW/kg whereas a goal of 80 kW/kg is stated for 2040. This paper systematically identifies the optimal BB dc-dc converter realization among a set of topologies with respect to weight and mission profile efficiency, considering cutting edge component technology, e.g., SiC power semiconductors and 3D printed complex geometry liquid cooled aluminum heatsinks. Two 15 kW demonstrator systems with wide-bandgap power semiconductors are built and extensively tested, i.e., an all-SiC 2-level 4-switch BB dc-dc converter with 44 kW/kg and an all-GaN 3-level 8-switch BB dc-dc converter with 86 kW/kg, thus complying with the 2040 power density target and exceeding state-of-the-art BB dc-dc converter systems by a factor of four with respect to gravimetric power density.

Index Terms—eVTOL, airborne, hybrid power supply, fuel cell, battery, dc-dc converter, non-isolated, buck-boost, gravimetric power density, ultra-lightweight.

I. INTRODUCTION

Urbanization is a megatrend of the 21st century with a projected 68% of the global population living in urban areas by 2050 [1]. The associated increase in population density will further intensify road traffic congestion and the associated productivity losses which already today are problematic and, e.g., in San Francisco result in a productivity loss of approximately half a million hours per day [2].

This boosts interest in Urban Air Mobility (UAM) utilizing the three-dimensional air space for transportation and allowing to bypass overcrowded streets [4], [5] with currently 250 companies conducting research [6] and a projected yearly market volume of 90 billion USD by 2050 [7]. UAM can be further categorized into intra-city (up to 50 km) and inter-city (up to and above 250 km) [7], [8]. In this context, all-electric Vertical Takeoff and Landing (eVTOL) aircraft allow to leverage the specific advantages of helicopters, i.e., vertical take-off and landing with low space requirements (**Fig. 1a.i**), and airplanes, i.e., energy efficient fixed-wing cruising (**Fig. 1a.ii**) [8]–[11].
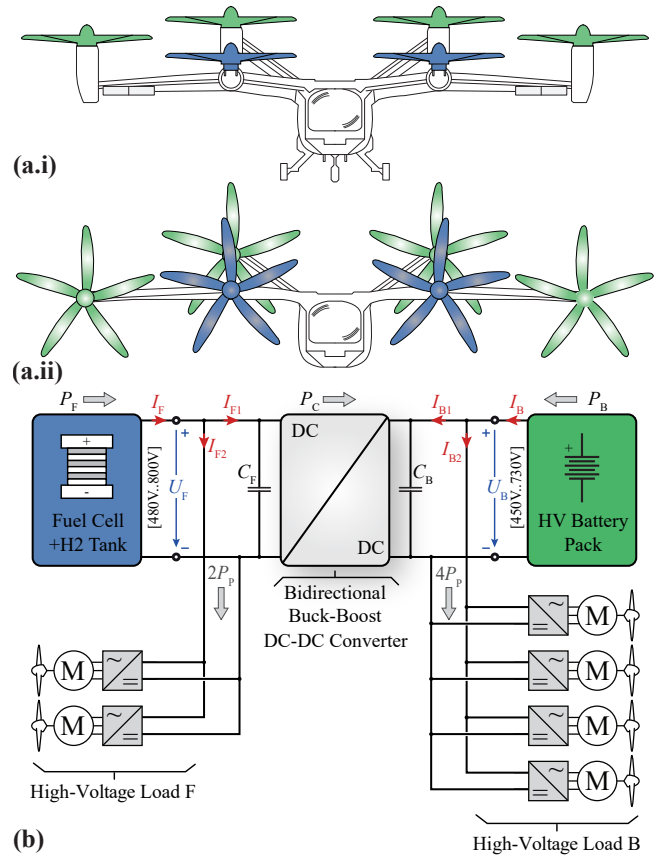
Fig. 1. (a) Illustration of an all-electric Vertical Takeoff and Landing (eVTOL) aircraft in (a.i) hover and (a.ii) fixed-wing cruise configuration (from [3]). (b) Considered hybrid battery-Fuel Cell (FC) power supply with an interconnecting Buck-Boost (BB) dc-dc converter regulating the power flow in between the two energy sources.

Advantageously, electric drive trains are highly efficient [12]–[16] and with an increase in sustainable electric energy generation (and thanks to air travel on a direct and/or straight trajectory towards the target destination) eVTOL aircraft may even compete with internal combustion and electric vehicles in terms of energy consumption and greenhouse gas emissions [17]–[19]. Further, electric motors with integrated drive inverter and gearbox are available today with gravimetric power densities of up to 12 kW/kg [20][1] and are thus competitive with state-of-the-art gas turbines [21], [22], and enable a lightweight

---

[1]Note that the volume and mass of an electric motor scale with the torque and thus lightweight motors feature high rotational speeds. The motor from [20] operates with up to 20 000 rpm and the gravimetric power density of 12 kW/kg includes the integrated inverter drive and a 6.7:1 gearbox to enable lower rotor speeds of up to 3000 rpm.
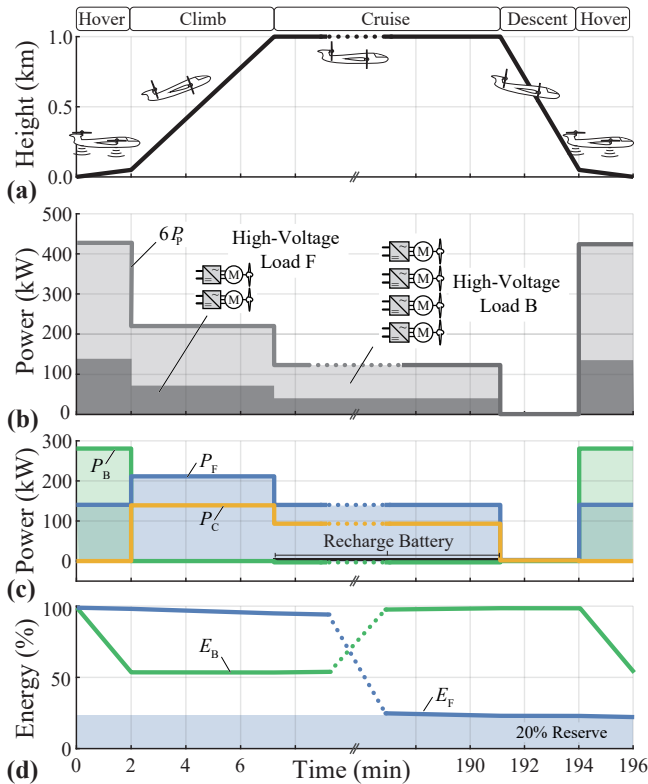
Fig. 2. Exemplary 800 km hybrid-power-supply eVTOL aircraft mission profile over time (details provided in **Appendix A**) displaying **(a)** altitude above ground, **(b)** total propulsion power demand $6P_P$ and load distribution between the FC- and the battery-side propulsion units, **(c)** instantaneous power flow of the FC P_F, the battery P_B and the dc-dc converter P_C, and **(d)** relative stored energy in the FC H_2-tank E_F (providing the bulk energy) and the battery E_B (providing the peak power capability when hovering).

distributed propulsion in eVTOL aircraft [9], [23][2]. Current research further aims at pushing electric motors beyond 15 kW/kg [23]–[27], and motor drive inverters are being pushed from 50 kW/kg [28]–[30] towards 80 kW/kg [31].
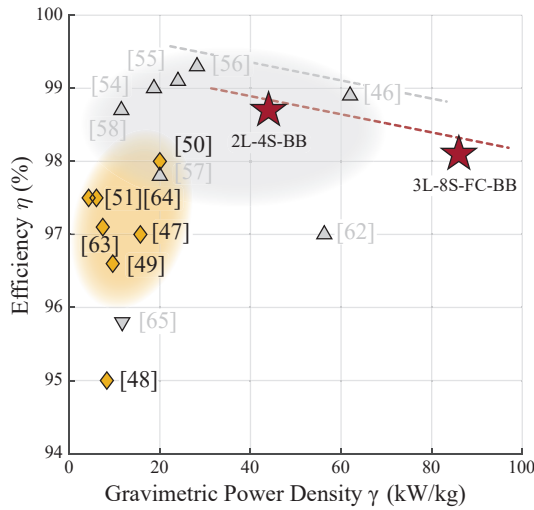
Although being highly efficient, purely battery-powered eVTOLs are limited to ranges below 200 km to 300 km due to the low gravimetric energy densities in the range of 200 Wh/kg to 300 Wh/kg of today's battery technology [10], [11], [32]–[36], which is inferior to kerosene with approximately 12 000 Wh/kg [12], [25]. When aiming at a further range extension, a hybrid battery-FC power supply architecture [10], [37]–[40] as highlighted in **Fig. 1b** is required, which includes an interfacing dc-dc converter regulating the power flow between the two energy sources which each power a set of inverter drives and electric motors for the propulsion. An exemplary 800 km flight trajectory is provided in **Fig. 2** (further details can be found in **Appendix A**): The propulsion power demand $6P_P$ is maximum during the hover take-off phase (**Fig. 1a.i**) and is largely provided by the battery pack featuring a high gravimetric power density but

limited energy storage capability. Subsequently, the eVTOL accelerates and transitions into the climb mode in fixed-wing-cruising configuration (**Fig. 1a.ii**) where the entire eVTOL power demand is covered by the FC and the dc-dc converter regulates the battery power to $P_B = 0$ to avoid a further depletion of the battery energy storage. Further, once the cruising height is reached, the battery can even be recharged with $P_B < 0$ such that the full battery capacity is available again for the landing. Thus, the high-pressure H_2-tank of the FC – featuring a high gravimetric energy density – serves as the bulk eVTOL energy storage [37], [38], [41]. Advantageously, refueling of the H_2-tank can be performed very rapidly, and the main deficiencies of the FC, namely the low response time and low gravimetric power density, can be compensated by the battery [21], [38], [41]–[43]. Note that a bidirectional realization of the interfacing dc-dc converter is required for the startup of the FC and for emergency mode.

Such a hybrid power supply, however, poses substantial stresses on the interfacing dc-dc converter which has to match the voltage levels U_F of the FC and U_B of the battery: The FC voltage U_F depends on the extracted power P_F and the battery voltage U_B depends on – among other parameters – the temperature, the state of charge and the age, such that a requirement of wide input-output voltage ranges results for the dc-dc converter. Here, the considered voltage ranges $U_F \in [480\,\text{V}, 800\,\text{V}]$ and $U_B \in [450\,\text{V}, 720\,\text{V}]$ correspond to a voltage variation of approximately a factor of two, and the overlapping input-output ranges require a dc-dc converter with step-up and step-down capability, i.e., a Buck-Boost (BB) converter, to interface the FC and the battery. In contrast to stationary (or also land-based mobility) applications, the system weight is of crucial importance in aviation and has a direct impact on energy consumption and the available payload of the aircraft, and thus gravimetric power density is a key metric for the Buck-Boost (BB) converter. Ultra-lightweight boost converter applications are well covered in the literature [44]–[46], and high gravimetric power densities of up to 60 kW/kg are reported [46] ([39] states a target power density of 80 kW/kg to be reached by 2040).

In contrast, BB dc-dc converter for hybrid electric power supply architectures [47]–[51], are understudied in the literature with previous work of the authors [52] investigating the converter weight limits based on theoretical considerations only. Hence, the goal of this paper is to systematically identify the optimal BB converter realization with respect to weight, efficiency and also system complexity from a set of converter topology candidates, and to provide experimental verification of the optimum realization's performance. The paper is structured as follows: **Sec. II-A** provides an overview of lightweight dc-dc converter systems described in the literature. **Sec. II-B-E** then summarize the considered converter specifications, the topology candidates and the employed multi-objective converter optimization procedure, with the results presented in **Sec. II-F**. Two converter prototypes are built and commissioned and details on the prototype systems are provided in **Sec. III-A**. Then, **Sec. III-B** provides comprehensive experimental verification of the functionality across the entire input-output voltage

---

[2]Electric drive trains have a relatively scale-free nature and can reach high gravimetric power density values irrespective of the rated power (in first approximation, i.e., if auxiliary components do not substantially impact the system volume, weight and losses), which represents a powerful Degree of Freedom (DOF) for distributed propulsion systems in eVTOL aircraft. In contrast, gas turbines reach optimal gravimetric power density only in the megawatt range [9], [23].

Fig. 3. Overview on ultra-lightweight dc-dc converter prototype systems in the literature comparing the achieved nominal efficiency η and gravimetric power density γ: the scatter symbols of systems providing only buck (downward pointing triangle) or only boost functionality (upward pointing triangle) are grayed out as they do not provide the buck-boost capability required for the hybrid power supply architecture in **Fig. 1b**. The two systems realized in this work, i.e., the 2-Level 4-Switch BB (2L-4S-BB) (**Fig. 5a**) and the 3-Level 8-Switch BB (3L-8S-FC-BB) (**Fig. 5b**) converter are represented by a star scatter symbol.

range, thereby verifying the theoretical considerations, and **Sec. III-C** provides an efficiency characterization of the converters. Last, **Sec. IV** summarizes the key findings of this publication.

II. ULTRA-LIGHTWEIGHT BUCK-BOOST DC-DC CONVERTERS

This section aims at investigating the gravimetric power density limits of BB dc-dc converters. First, results from a literature research on lightweight boost and BB converters are presented. Subsequently, the considered specifications for the system optimization and the investigated converter topologies are discussed. Last, a comprehensive multi-objective optimization procedure is introduced and the topologies' Pareto fronts with respect to the gravimetric power density γ and the weighted mission profile / drive cycle efficiency $\bar{\eta}$ are compared.

A. Gravimetric Power Density Limits of DC-DC Power Converters

There exists a large number of publications on weight optimization for ultra-lightweight and highly compact boost converters for mobile and/or airborne applications [44]–[46], [50], [53]–[62]. **Fig. 3** presents an overview of achieved efficiency and gravimetric power density values. There, ultra-high gravimetric power densities of up to 60 kW/kg are reported [46], [62] and [39] states a target power density of 80 kW/kg to be reached by the year 2040.

In contrast, lightweight BB dc-dc converters are an understudied topic with fewer publications available in the literature [47]–[51]. Gravimetric power density values of up to
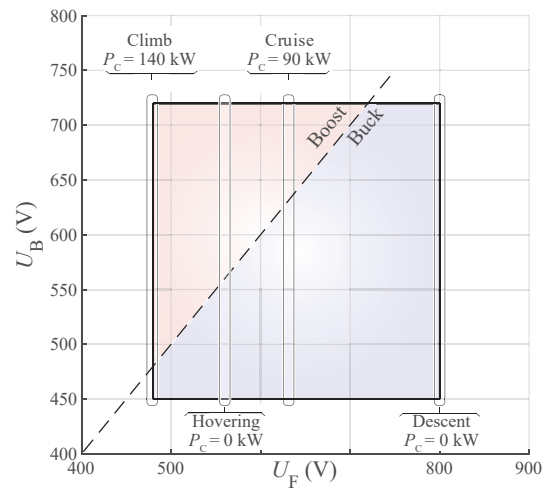
Fig. 4. Considered input U_F and output U_B voltage ranges of the dc-dc converter depicted in **Fig. 1b**. The FC voltage is predominantly power dependent and the resulting FC voltage U_F and dc-dc converter power P_C levels for hovering ($U_F = 560$ V, $P_C = 0$ kW), climbing ($U_F = 480$ V, $P_C = 140$ kW), cruising ($U_F = 620$ V, $P_C = 90$ kW) and descent ($U_F = 800$ V, $P_C = 0$ kW) are highlighted. In contrast, the battery voltage U_B depends on – among others – the state of charge, temperature and number of past charge-discharge cycles, i.e., in contrast to U_F, U_B is not a-priori known from the eVTOL aircraft operating point, and the full battery voltage range $U_B \in [450\,\text{V}, 720\,\text{V}]$ has to be considered for each of the flight modes.

20 kW/kg [50] are documented (**Fig. 3**) and the large input-output voltage ranges in hybrid FC-battery electric power supply architectures pose substantial stresses on the power components. However, [52] predicts BB dc-dc converters power density values of up to 60 kW/kg (i.e., similar to the limits of boost-only systems) based on a Pareto optimization but does not provide experimental verification. Hence, in the following the goal is to systematically identify and experimentally verify the optimal BB converter realization with respect to weight and efficiency.

B. Considered Specifications

Both FCs and batteries feature a dc output voltage varying in a wide range thus posing substantial stresses on the interfacing dc-dc converter. For the FC the voltage U_F depends mainly on the extracted power P_F and in contrast the battery voltage U_B depends on – among other parameters – the temperature, the state of charge and the hours in operation / age, i.e., is not directly defined by the operating point.

Fig. 4 highlights the voltage ranges of the FC $U_F \in [480\,\text{V}, 800\,\text{V}]$ and of the battery $U_B \in [450\,\text{V}, 720\,\text{V}]$ considered in this paper, both varying by nearly a factor of two. There, the dashed line represents the boundary between step-up/boost and step-down/buck operation and thus a standard boost-type converter (with the output voltage U_B limited to values strictly larger than the input voltage U_F) cannot be employed to interface the FC and the battery. The considered mission profile in **Fig. 2** results in a BB dc-dc converter power of up to $P_C = 140$ kW. To assure sufficient margin the nominal power is set to $P_C = 150$ kW which has to be delivered throughout the entire input-output voltage

range $U_F \in [480\,\mathrm{V}, 800\,\mathrm{V}]$ and $U_B \in [450\,\mathrm{V}, 720\,\mathrm{V}]$. The nominal power is realized by paralleling ten converter modules with $P_M = 15\,\mathrm{kW}$ which enables redundancy [52], [66] and the use of power transistors in low-inductive, high-performance packages. Further, the converter is required to allow bidirectional power flow such that power can be fed from the battery to the FC during system start-up or in case of emergency operation.

For the assessment of the mission profile efficiency $\bar{\eta}$, a set of characteristic operating points of the different flight phases shown in **Fig. 2** is considered (more details on the mission profile and the resulting power requirements for the dc-dc converter are provided in **Appendix A**). As discussed, the battery voltage is – in contrast to the FC voltage – not a-priori known for a given operating point and therefore, a set of equally spaced voltages of $U_B \in [450\,\mathrm{V}, 720\,\mathrm{V}]$ is considered to calculate an average efficiency for each of the flight phases, which are:

- **Hovering:** the FC and the battery each power the connected propulsion units, such that no power is processed by the dc-dc converter; accordingly this operating point is ignored with respect to the calculation of $\bar{\eta}$.
- **Climbing:** the dc-dc converter is required to transfer a high power $P_C = 140\,\mathrm{kW}$ from the minimum FC voltage $U_F = 480\,\mathrm{V}$ (and $U_B \in [450\,\mathrm{V}, 720\,\mathrm{V}]$) to the propulsion units on the battery side. This operating point is attributed with a weight $\alpha_1 = 50\%$ to calculate $\bar{\eta}$.
- **Cruising:** the dc-dc converter processes a reduced power level $P_C = 90\,\mathrm{kW}$ during the entire cruising phase. There, the FC voltage recovers to $U_F = 640\,\mathrm{V}$ (due to the reduced load). This operating point is attributed with a weight $\alpha_2 = 50\%$ to calculate $\bar{\eta}$.
- **Descent:** the power requirement during this phase is minimal and this operating point is ignored with respect to the calculation of $\bar{\eta}$.

Finally, the overall mission profile efficiency is calculated as $\bar{\eta} = \alpha_1 \bar{\eta}_1 + \alpha_2 \bar{\eta}_2$.

C. Considered Topologies

Fig. 5 shows the four BB dc-dc converter topologies considered in the multi-objective Pareto optimization: In the most simple case, a 2L-4S-BB converter realization [67], [68] is considered. This low-complexity, low-component-count approach is depicted in **Fig. 5a** and comprises an input capacitor C_F, buck-stage transistors T_F/T_F', boost-stage transistors T_B/T_B', and a BB inductor L. The simplicity of this topology comes at the cost of substantial hard-switching losses in the 1200 V Silicon Carbide (SiC) power transistors required to cover the half-bridge voltage stresses of up to 800 V, and high High-Frequency (HF) stresses on the BB inductor L. Advantageously, a quasi-single-stage operation [69] is considered here: In step-down operation, only the buck half-bridge T_F/T_F' is switched with Pulse-Width Modulation (PWM) and the boost-stage high-side switch T_B is permanently on, thus connecting the switch node $\bar{B}$ to the battery-side output terminal B. The modulation is inverted for step-up mode, thus resulting in a substantial reduction of the hard-switching losses and Sec. II-D discusses the required control structure and measurements in more detail.

(a)   **(b)**

(c)   **(d)**
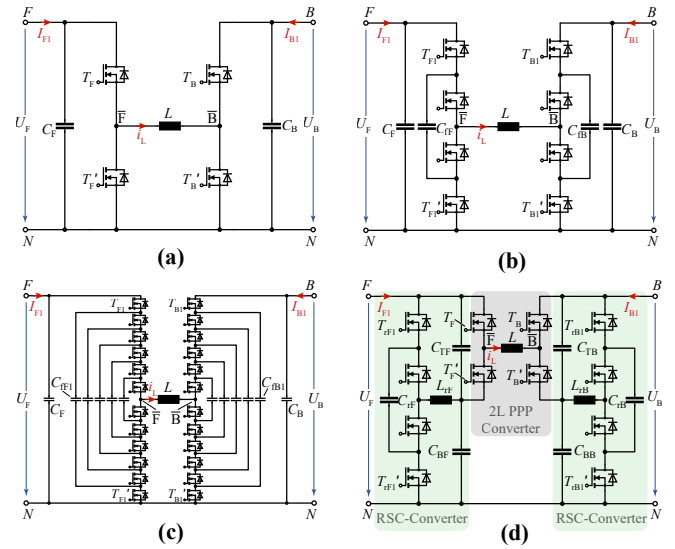
Fig. 5. Considered topologies for the realization of the BB converter interconnecting the FC and the battery of the hybrid power supply architecture in **Fig. 1b**: **(a)** 2-Level 4-Switch BB (2L-4S-BB) converter (both, a standard hard-switched and an advanced Constant-Frequency (CF) Zero-Voltage-Switching (ZVS) modulation are considered), **(b)** 3-Level 8-Switch BB (3L-8S-FC-BB) converter, **(c)** 7-Level 24-Switch BB (7L-24S-FC-BB) converter, and **(d)** Resonant Switched Capacitor 12-Switch BB (RSC-12S-BB) converter. Details on the characteristic waveforms of the converter concepts within the considered input-output voltage ranges of **Fig. 4** can be found in [52].

Alternatively, the buck- and the boost-stage can be switched simultaneously by means of an advanced modulation scheme resulting in a trapezoidal BB inductor current, which reverses its direction in each switching period and thus enables Constant-Frequency (CF) Zero-Voltage-Switching (ZVS) [70], [71] with substantially reduced power semiconductor losses even at high switching frequencies.

Flying capacitor multi-level bridge-legs feature an increased effective switching frequency and a higher voltage-level count such that the BB inductor Voltage-Time Area (VTA) decreases quadratically with increasing level count, which enables a substantial reduction of the BB inductor volume and weight [56], [72]–[74]. Further, the required blocking voltage rating of the power semiconductors reduces and allows the use of power transistors with improved figure of merits (compared to a 2L-4S-BB converter realization with 1200 V SiC power transistors [75]). For the considered FC and battery voltage ranges, the 3-Level 8-Switch BB (3L-8S-FC-BB) converter (**Fig. 5b** with one flying capacitor in each bridge-leg) and the 7-Level 24-Switch BB (7L-24S-FC-BB) converter (**Fig. 5c** with five flying capacitor in each bridge-leg) are considered as they advantageously allow the use of 650 V and 200 V Gallium Nitride (GaN) power semiconductors, respectively. Note that the flying capacitor voltages are balanced passively because the BB inductor current equally charges and discharges the flying capacitors within a switching period [72], [73], [76], [77].

Another promising concept discussed in the literature are the so-called Partial Power Processing (PPP) converters [53], [57], [78]–[81], where ideally only a small share of the total transferred power is processed by an isolated dc-dc converter. In the case at hand, however, the input and

output voltages vary by a factor of two, which would require the isolated dc-dc converter to be dimensioned for approximately 50% of the nominal system power. Therefore, the non-isolated Resonant Switched Capacitor 12-Switch BB (RSC-12S-BB) PPP converter concept from [82]–[84] is considered. Each converter stage then features a resonant symmetrizer (see **Fig. 5d**) with, e.g., in the buck stage, a three-level flying capacitor bridge leg, a resonant inductor L_{rF} and a split dc-link with capacitors C_{TF} and C_{BF} which are both symmetrized to half the input voltage U_F). Thus, the corresponding 2L-4S-BB PPP converter only processes half the transferred power and advantageously all power semiconductors of this topology can be realized with high-performance 650 V GaN power transistors. Note that this topology is strictly limited to a conversion ratio below a factor of two, which is compatible with the considered voltage ranges in **Fig. 4**.

D. Quasi-Single-Stage Control

As discussed in **Sec. II-C** the aim is to operate the considered topologies in **Fig. 5** in a quasi-single-stage mode with a mutually exclusive operation of the buck and the boost stage. **Fig. 6** depicts the considered control diagram for the 2L-4S-BB converter where the BB dc-dc converter power reference P_C^* (set depending on the flight phase; see **Appendix A**) is translated into a battery-side output current reference I_{B1}^* which is controlled indirectly: The battery-side current reference I_{B1}^* is translated into a buck-boost inductor current reference i_L^* by taking into account the feed-forward boost stage duty cycle d_B^* obtained from the measured FC input U_F and battery output voltage U_B. The output signal u_L^* of the current controller R_L is then fed into the modulator block from [85], [86] which assures the mutually exclusive operation of the buck and the boost stage. The modulator block further assures a smooth transition from buck to boost operation and vice versa. The resulting buck d_F and boost duty cycles d_B for a small control error (i.e., $u_L^* \approx 0$) are indicated across the entire input-output voltage range where a unity duty cycle corresponds to a high-side switch which is permanently in the on state.

Apart from the input-output voltage and the buck-boost inductor measurements, further the input and output currents have to be measured to allow for over-current protection and the total number of required measurements for the 2L-4S-BB converter are indicated in **Tab. I**. The control diagram in **Fig. 6** is also applicable for the other considered topologies in **Fig. 5** where additional voltage and current measurements, e.g., of flying-capacitor voltages, are required to assure safe operation of the converter systems.

Note that due to the presence of an energy storage on both, the input (FC) and the output side (battery), and the slow dynamics of the aircraft with smooth transitions between, e.g., hovering and fixed-wing cruising configuration, the control bandwidth requirements for the buck-boost dc-dc converter in a hybrid power supply are also relatively low compared to applications where a dc output voltage needs to be tightly regulated in the presence of abrupt load steps. Therefore, the controller tuning is not detailed herein; standard methods are applicable and described in the literature, e.g., [85], [87], [88].
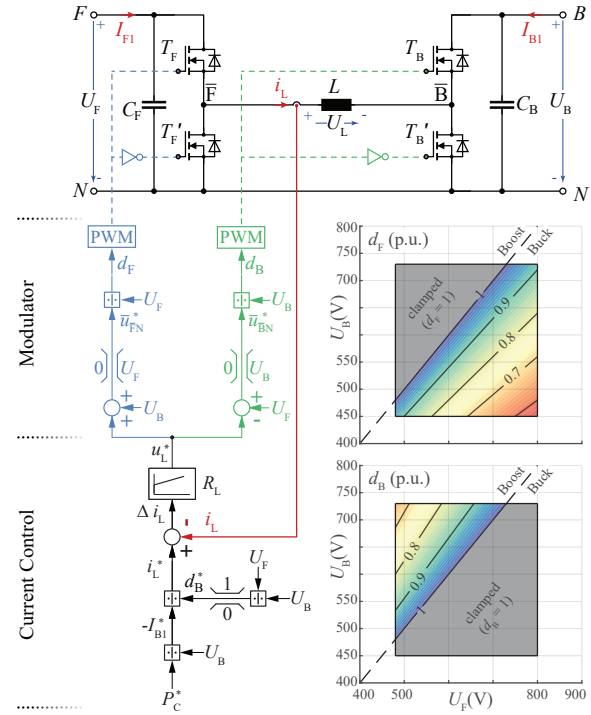
Fig. 6. Considered control diagram for the quasi-single-stage operation of the 2L-4S-BB converter in **Fig. 5a**: The BB dc-dc converter power reference P_C^* is translated into a battery-side current reference I_{B1}^* and a buck-boost inductor current reference i_L^* by taking into account the output voltage U_B and the feed-forward boost stage duty cycle d_B^* obtained from the FC input U_F and battery output voltage U_B, respectively. The output signal u_L^* of the current controller R_L is then fed into the modulator from [85], [86] block which assures the mutually exclusive operation of the buck and the boost stage. The resulting buck d_F and boost duty cycles d_B for a small control error (i.e., $u_L^* \approx 0$) are indicated across the input-output voltage range where a unity duty cycle corresponds to a high-side switch which is permanently in the on state. Note that here the duty cycle definition from [85] is considered where d_B represents the relative on-time of the high-side switch T_B and the boost-switch T_B' is switched complementary.

TABLE I

REQUIRED VOLTAGE AND CURRENT MEASUREMENTS FOR THE CONSIDERED TOPOLOGIES IN **FIG. 5.**

Topology	2L-4S-BB	3L-8S-FC-BB	7L-24S-FC-BB	RSC-12S-BB
Volt. Meas.	2	4	12	6
Curr. Meas	3	3	3	5

E. Converter Optimization

It is important to highlight that the topologies depicted in **Fig. 5** are known and well described in the literature. However, a systematic comparison of the relevant performance metrics for an eVTOL aircraft is not yet available. Therefore, to identify the optimal BB dc-dc converter topology and converter realization with respect to weight and mission profile efficiency, a comprehensive Pareto optimization [52], [53], [82], [89] is conducted.

The optimization routine is based on [52] (which also provides a flow-graph representation of the procedure) and takes into account all relevant DOF for the converter realization: The main converter-level DOF, e.g., switching frequency f_s and the single-side peak BB inductor current ripple ΔI_L
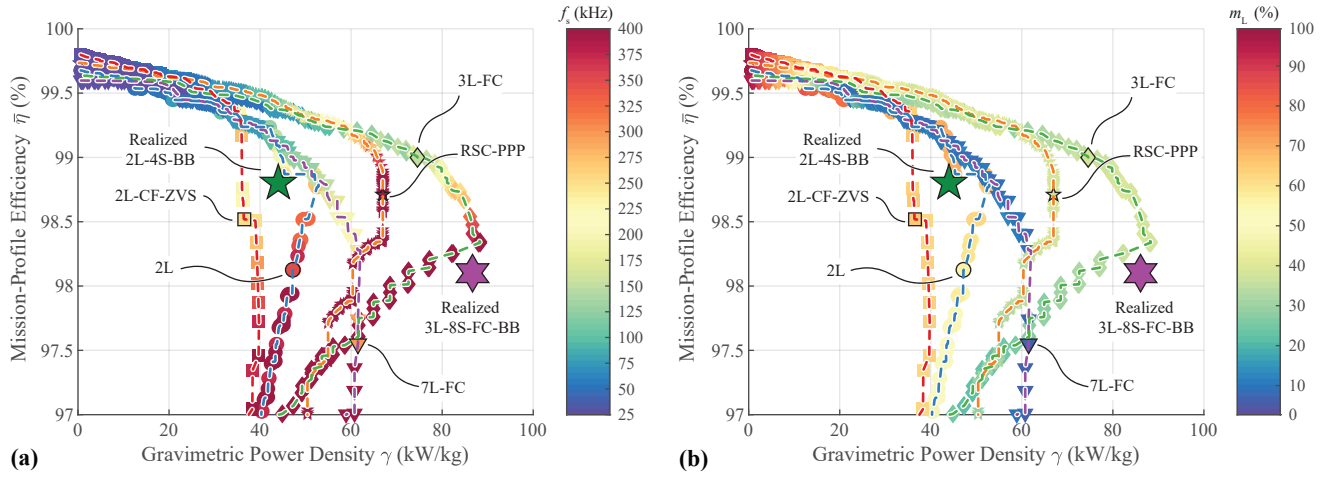
Fig. 7. Pareto optimization results comparing the performance limits of the BB converter interconnecting the FC and the battery of the hybrid power supply architecture in **Fig. 1b** in terms of gravimetric power density γ and weighted mission-profile / drive-cycle efficiency $\bar{\eta}$ of the considered topologies in **Fig. 5**, i.e., the 2L-4S-BB and the CF-ZVS 2L-4S-BB, the 3-Level 8-Switch BB (3L-8S-FC-BB) and the 7-Level 24-Switch BB (7L-24S-FC-BB), as well as the Resonant Switched Capacitor 12-Switch BB (RSC-12S-BB) converter: The scatter point color indicates in **(a)** the switching frequency f_s and in **(b)** the relative mass contribution m_L of the magnetics to the overall converter system's mass. The two realized BB converter systems are highlighted by stars and achieve an experimentally verified (see **Section III**) performance of $\bar{\eta} = 98.8\%$ and $\gamma = 44\,\mathrm{kW/kg}$ for the 2L-4S-BB converter, and $\bar{\eta} = 98.1\%$ and $\gamma = 86\,\mathrm{kW/kg}$ for the 3L-8S-FC-BB converter.

(defined as a percentage of the maximum DC inductor current which is translated into a buck-boost inductor value L) are swept individually in a wide range. The required input and output capacitor values are calculated based on a peak-to-peak voltage ripple criterion $\Delta U_{\mathrm{pp}} = 5\,\%$ relative to the maximum capacitor voltage. Each value pair of $(f_s, \Delta I_L)$ has unique characteristic converter voltage and current waveforms and suitable component realizations are subsequently assessed.

To do so, the component level DOFs are swept: For the power semiconductors different materials (SiC, GaN), voltage ratings (based on the topology; see **Sec. II-C**) and different numbers of paralleled devices (i.e., different chip areas are considered, which impact the semiconductor hard-switching and conduction losses). Magnetic components offer the largest number of DOFs [90] as core geometries and core sizes (TDK N87 E and ELP cores are considered; for a given core size several cores can be stacked to increase the core cross section), the airgap length, the number of turns as well as the winding realization (solid enamelled and litz wire with varying strand diameter and number) can be combined. For the capacitors, ultra-compact anti-ferroelectric Multilayer Ceramic Capacitors (MLCCs) [91] are considered which are available for different voltage ratings (based on the topology; see **Sec. II-C**) and the number of parallel devices is selected to meet the required capacitor value.

In a first step, the losses of each component realization are calculated for nominal power operation within the entire input-output voltage range. Invalid component realizations (e.g., with excessive losses/temperatures or magnetic core saturation) are omitted and in a second step, the mission profile performance is calculated. For the modeling of the component losses, calorimetrically measured [92] semiconductor hard- and soft-switching losses from [52], [75], [93], [94] are employed, the inductor magnetic core

and winding losses are calculated according to [90], and the capacitors losses are assessed based on the datasheet and including sufficient derating for the bias-voltage-dependent loss behavior [91], [95]. The cooling system considers water cooling (maximum inflow temperature of $80\,°\mathrm{C}$; a maximally acceptable power semiconductor junction temperature of $T_j = 150\,°\mathrm{C}$ is defined) using ultra-lightweight 3D-printed aluminum cold plates with semiconductors attached on both sides [52], [59], [61].

Next, a large number of converter realizations for a single value pair of converter specifications $(f_s, \Delta I_L)$ is obtained by recombining the corresponding realizations of each power component (e.g., for the 2L-4S-BB converter a suitable half-bridge realization can be freely combined with any of the buck-boost inductor and input / output capacitor realizations). Given the very similar voltage ranges of the FC (U_F) and the battery (U_B), only identical buck and boost stages (i.e., same components and switching frequency) are considered for a converter realization. Last, for each converter realization the mission profile efficiency and the system weight can be obtained by adding up the contributions of the individual power component realizations.

F. Converter Optimization Results

As discussed in **Sec. II-B**, the nominal BB dc-dc converter power $P_C = 150\,\mathrm{kW}$ is realized by paralleling ten converter modules with $P_M = 15\,\mathrm{kW}$ and only a single module is considered here. **Fig. 7** presents the Pareto fronts (mission-profile efficiency versus gravimetric power density) obtained from the multi-objective optimization of the considered BB topologies in **Fig. 5**. The scatter point color **Fig. 7a** highlights the switching frequency of each converter realization, and the well-known trend of increasing gravimetric power density γ (decreasing passive component weight) and decreasing efficiency $\bar{\eta}$ (increasing switching losses) with increasing switching frequency can be observed [96].

The optimization predicts extreme power densities $\gamma > 40\,\mathrm{kW/kg}$ at high efficiencies $\bar{\eta} > 98.5\%$ even for the standard hard-switched 2L-4S-BB topology. The relative mass contribution m_L of the magnetic components (here the BB inductor) on the overall converter weight is presented in **Fig. 7b**: Given the lightweight realization of the capacitors with CeraLink MLCCs [91] and of the cooling system with 3D-printed aluminum cold plates, the BB inductor has a dominant weight share in the converter which cannot be pushed below $m_\mathrm{L} = 60\%$ even for extremely high switching frequencies around $f_\mathrm{s} = 400\,\mathrm{kHz}$. Note that the employed liquid cooling does not lead to an immediate weight penalty for high switching losses (in contrast to forced convective cooling where the cooling system volume and weight increases in first approximation linearly with the semiconductor losses), which is advantageous for this hard-switched topology.

The 2L-4S-BB topology with CF-ZVS modulation enables converter realizations with outstanding efficiencies beyond 99% but power density is limited to values below those of the hard-switched 2L-4S-BB converter. This different characteristics can be explained by two factors: First, the trapezoidal BB inductor current waveforms with polarity reversal imposes a high HF peak-to-peak inductor current variation with associated HF winding conduction losses and magnetic core losses, thus resulting in large, thermally limited inductor designs with the size determined by the losses [97]. Second, the low switching losses as a main advantage of the CF-ZVS modulation do not enable a weight reduction in the cooling system compared to the standard hard-switched 2L-4S-BB converter (as would be the case for forced convection cooling).

With the effective switching frequency doubling and the inductor voltage level cut in half, the 3L-8S-FC-BB topology enables a more compact and lightweight realization of the dominant BB inductor compared to the 2L-4S-BB topology, and outstanding power densities beyond $\gamma = 80\,\mathrm{kW/kg}$ are predicted by the optimization, with low mass shares of the inductor of $m_\mathrm{L} < 30\%$. Note that this exceeds the performance calculated earlier in [52], because here, new prototype ultra-low on-state resistance 650 V GaN power semiconductors are included in the optimization (more details are provided in **Sec. III**). In contrast, the 7L-24S-FC-BB topology is limited to power density values of around $\gamma = 60\,\mathrm{kW/kg}$ only. Note that thanks to the further increase of effective switching frequency and number of voltage levels, the relative mass contribution m_L of the magnetic components (**Fig. 7b**) is further reduced substantially compared to the 3L-8S-FC-BB topology and pushed from $m_\mathrm{L} = 30\%$ to below $m_\mathrm{L} = 10\%$. However, now other converter components become dominant with respect to the total weight. Specifically, the large number of semiconductors (and the thus needed larger coldplate) and the flying capacitors prevent 7L-24S-FC-BB converter realizations from outperforming the 3L-8S-FC-BB topology.

Last, the RSC-12S-BB topology enables also outstanding efficiency and power density values towards $\gamma = 70\,\mathrm{kW/kg}$. Similar to the 7L-24S-FC-BB topology, the large number of active and passive components for the two resonant symmetrizers limits the maximum achievable converter power density.

TABLE II
DETAILS OF THE EMPLOYED MAIN 2L-4S-BB AND 3L-8S-FC-BB CONVERTER COMPONENTS.

	2L-4S-BB	3L-8S-FC-BB
Meas.	$\bar{\eta} = 98.8\%$ $\gamma = 44\,\mathrm{kW/kg}$ $\rho = 82\,\mathrm{kW/dm^3}$ Weight: 346 g	$\bar{\eta} = 98.1\%$ $\gamma = 86\,\mathrm{kW/kg}$ $\rho = 108\,\mathrm{kW/dm^3}$ Weight: 175 g
Semicond.	Cree C3M0016120K 1.2 kV SiC / 16 mΩ $P_\mathrm{max} = 150\,\mathrm{W}$[2] $f_\mathrm{s} = 275\,\mathrm{kHz}$	Infineon Technologies[1] 650 V GaN / max. 21 mΩ $P_\mathrm{max} = 106\,\mathrm{W}$[2] $f_\mathrm{s} = 400\,\mathrm{kHz}$ $f_\mathrm{s,eff} = 800\,\mathrm{kHz}$
Inductor	$L = 13.4\,\mathrm{\mu H}$ ($\Delta I_\mathrm{L} = 75\%$) 2x ELP 43/10/28, N87 Airgap: 2mm 6x turns / 4600x 40 μm Litz wire	$L = 7.5\,\mathrm{\mu H}$ ($\Delta I_\mathrm{L} = 25\%$) 3x ELP 22/6/16, N87 Airgap: 0.4mm 4x turns / 2.6 mm Solid wire
DC-Cap.	$C_\mathrm{F} = C_\mathrm{B} = 0.75\,\mathrm{\mu F}$ ($\Delta U_\mathrm{pp} = 5\%$) 3x TDK CeraLink B58031U9254M062 (900 V / 0.25 μF)	$C_\mathrm{F} = C_\mathrm{B} = 1\,\mathrm{\mu F}$ ($\Delta U_\mathrm{pp} = 5\%$) 4x TDK CeraLink B58031U9254M062 (900 V / 0.25 μF)
Fly. Cap.	-	$C_\mathrm{fF} = C_\mathrm{fB} = 1\,\mathrm{\mu F}$ ($\Delta U_\mathrm{pp} = 5\%$) 1x TDK CeraLink B58031U5105M062 (500 V / 1 μF)
Control	Texas Instruments TMS320C2834X 32-bit MCU, 300 MHz	

[1]The hard- and soft-switching losses are calculated assuming two parallel connected IGOT60R042D1 dies with data from [52].
[2]Resulting for a maximum junction temperature of $T_\mathrm{j} = 150\,°\mathrm{C}$, a maximum coldplate inflow temperature of 80 °C and a high-performance Thermal Interface Material (TIM) with 17.8 W/(mK) and 0.5 mm thickness.

Thus the 3L-8S-FC-BB topology represents a sweet-spot concept between component stresses and system complexity and allows an optimal system realization with respect to maximum gravimetric power density at still competitive efficiency.

III. EXPERIMENTAL VERIFICATION

To verify the findings of the Pareto optimization, a 2L-4S-BB and a 3L-8S-FC-BB 15 kW BB dc-dc converter prototypes are built . Note that for the realization of a compact (and thus lightweight) converter prototype system, matching power component form factors are of great importance. Thus, the converter design selection process includes manual scanning of a large number of converter designs in the close vicinity of the topology Pareto front to identify the optimum design with respect to practical considerations. The performance of the realized demonstrators is indicated in **Fig. 3** and in **Fig. 7**.

A. Converter Prototype Systems

First, considering the simplicity of the topology, a hard-switched 2L-4S-BB converter with $\bar{\eta} = 98.8\%$ and $\gamma = 44\,\mathrm{kW/kg}$ is realized and **Fig. 8a** highlights the system structure and the assembled prototype. **Tab. II** provides details on the main system specifications and power components: The converter employs a high switching frequency
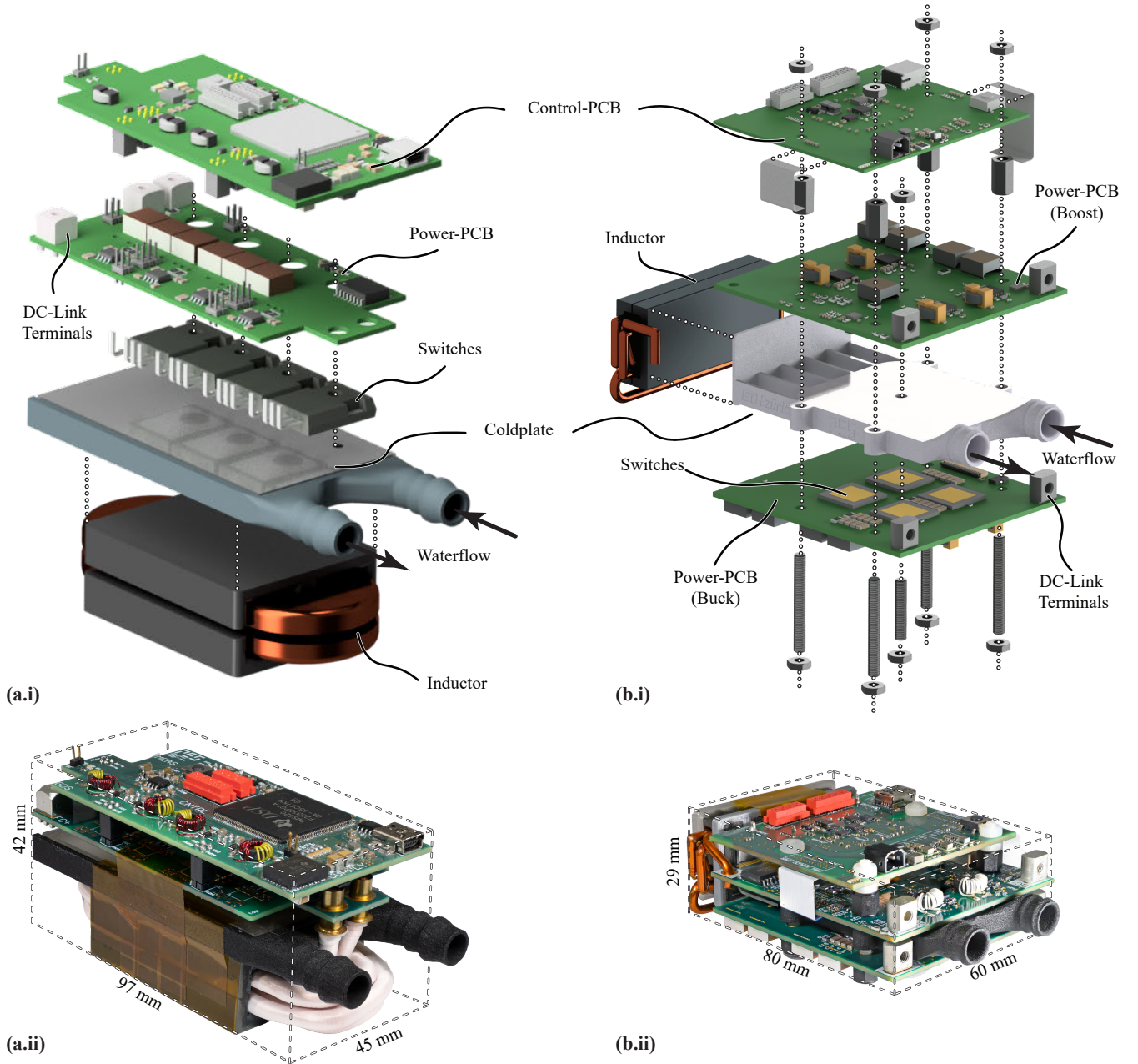
Fig. 8. Realized 15 kW prototype systems of the BB converter interconnecting the FC and the battery of the hybrid power supply architecture in **Fig. 1b**: **(a.i)** 3D-CAD rendering and **(a.ii)** photo of the realized 2L-4S-BB converter with $\bar{\eta} = 98.8\%$ and $\gamma = 44\,\mathrm{kW/kg}$; **(b.i)** 3D-CAD rendering and **(b.ii)** photo of the realized 3L-8S-FC-BB converter with $\bar{\eta} = 98.1\%$ and $\gamma = 86\,\mathrm{kW/kg}$. Details on the employed components are provided in **Tab. II** and **Fig. 9** provides the weight distribution among the components.

of $f_s = 275\,\mathrm{kHz}$ and the large (single-side) maximum HF inductor current ripple of $\Delta I_L = 75\%$ (relative to the maximum DC inductor current) reduces the hard-switching turn-on current values in the four $16\,\mathrm{m\Omega}$, $1.2\,\mathrm{kV}$ SiC power semiconductors.

Fig. 9 further presents the measured converter weight with a relative magnetic weight contribution of $m_L = 65\%$. Note that the calculated total mass from **Sec. II** is exceeded by approximately 15% which is mainly due to a higher-than-expected inductor core weight of $32\,\mathrm{g}$ (which was calculated using the datasheet dimensions), such that the realized prototype is located slightly behind the Pareto front in **Fig. 7**.

The second BB prototype system is the 3L-8S-FC-BB converter in **Fig. 8b** with $\bar{\eta} = 98.1\%$ and an unprecedented power density of $\gamma = 86\,\mathrm{kW/kg}$ (see **Fig. 3**). Here, the buck and the boost stage of the converter are realized with two identical power PCBs which are attached to the same coldplate. The converter employs a switching frequency of $f_s = 400\,\mathrm{kHz}$ (resulting in an effective switching frequency of $f_{s,\mathrm{eff}} = 800\,\mathrm{kHz}$) for the total of eight $21\,\mathrm{m\Omega}$, $650\,\mathrm{V}$ GaN power semiconductors from Infineon Technologies. Here, the low hard-switching losses of GaN transitors enable to select a lower maximum HF inductor current ripple of $\Delta I_L = 25\%$, and the increased effective switching frequency and number of voltage levels result in a relative
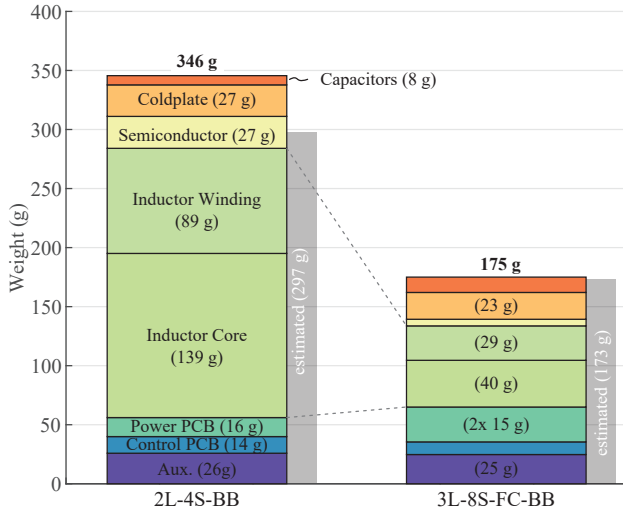
Fig. 9. Measured weight distribution of the 2L-4S-BB ($\gamma = 44\,\text{kW/kg}$) and 3L-8S-FC-BB ($\gamma = 86\,\text{kW/kg}$) converter prototypes in **Fig. 8**. The gray boxes represent the weight estimate obtained from the multi-objective Pareto optimization results in **Fig. 7** for the converter designs, which closely matches the realized prototypes. Note that the 2L-4S-BB converter's weight is primarily dominated by the buck-boost inductor representing approximately 65% of the total converter mass; in contrast, the 3L-8S-FC-BB converter's weight is more evenly distributed among the main power components.

magnetic weight contribution of $m_\text{L} = 40\%$ (see **Fig. 9**) and a total weight reduction of 50% compared to the 2L-4S-BB converter prototype. It is important to highlight that the passive balancing of the flying capacitors was found to be insufficient (due to the low flying capacitor values selected based on a 5% peak-to-peak HF voltage ripple criterion only) and thus an active correction-duty-cycle-based capacitor voltage controller according to [98] was implemented. Further it's interesting to highlight that the power stage (i.e., the converter without the control PCB) features a mass of only 159 g thus indicating that future BB dc-dc converter designs with high integration may even break through the $100\,\text{kW/kg}$ barrier.

It is worth mentioning that – although a low converter volume is not the primary goal of the optimization – high volumetric power density values of $\rho = 82\,\text{kW/dm}^3$ and $\rho = 108\,\text{kW/dm}^3$ are achieved for the 2L-4S-BB and the 3L-8S-FC-BB converter, respectively, where the difference in volume is less accentuated than the difference in weight due to the different form factors of the two prototype systems.

B. Experimental Converter Waveforms

Both prototype systems are extensively tested and **Figs. 10a,b** depict nominal power ($P_\text{M} = 15\,\text{kW}$) oscilloscope screenshots for the 2L-4S-BB and the 3L-8S-FC-BB converter, respectively. Note that an adjustable resistor bank is connected to the battery output side to adjust the power flow for a given output voltage level. To monitor self-heating of relevant power components in the prototype systems, several thermocouples were located in the device under test. Due to the efficient liquid cooling unit, all recorded temperatures safely remained below $100\,^\circ\text{C}$ for both systems.

In **Figs. 10a.i,b.i**, the maximum FC input voltage $U_\text{F} = 800\,\text{V}$ is stepped down to the minimum battery output voltage $U_\text{B} = 450\,\text{V}$ and with the considered quasi-single-stage modulation the boost-stage switch-node $\bar{B}$ is connected by the corresponding high-side semiconductor(s) to the battery-side output terminal B and $u_{\bar{B}\text{N}} = U_\text{B}$ such that the average inductor current is equal to the battery-side output current $\bar{i}_\text{L} = -I_{\text{B}1}$. At the same time the buck stage semiconductors are switched at HF: For the 2L-4S-BB converter a switch node voltage $u_{\bar{F}\text{N}} = \in \{0, U_\text{F}\}$ at a switching frequency of $f_\text{s} = 275\,\text{kHz}$ is generated, resulting in the maximum VTA for the considered voltage ranges applied to the BB inductor and a large HF inductor current ripple causing a notable HF voltage ripple on the battery-side output voltage $u_{\bar{B}\text{N}} = U_\text{B}$. In contrast, the 3L-8S-FC-BB converter generates a switch node voltage $u_{\bar{F}\text{N}} = \in \{U_\text{F}/2, U_\text{F}\}$ at an effective switching frequency of $f_{\text{s,eff}} = 800\,\text{kHz}$, resulting in a substantially reduced VTA applied to the BB inductor with a smaller HF inductor current ripple. Thus the HF voltage ripple on the battery-side output voltage $u_{\bar{B}\text{N}} = U_\text{B}$ is substantially reduced compared to the 2L-4S-BB converter.

In **Figs. 10a.ii,b.ii**, the minimum FC input voltage $U_\text{F} = 480\,\text{V}$ is stepped up to the maximum battery output voltage $U_\text{B} = 720\,\text{V}$ and the buck-stage switch-node $\bar{F}$ is connected by the corresponding high-side semiconductor(s) to the battery-side input terminal F and $u_{\bar{F}\text{N}} = U_\text{F}$. Note that now the average inductor current is strictly larger than the battery-side output current $\bar{i}_\text{L} > -I_{\text{B}1}$ and, the HF inductor current ripple causes an HF voltage ripple on the FC-side input voltage $u_{\bar{F}\text{N}} = U_\text{F}$.

C. Efficiency Characterization

The converter operating behavior is further systematically evaluated throughout the entire input-output voltage range from **Fig. 4**. Thus, **Fig. 11** presents the power conversion efficiency η recorded with a Norma D6100 power analyzer as a function of the FC input U_F and the battery output voltage U_B and for four different power levels. A peak efficiency $\eta = 99.1\%$ ($U_\text{F} = 480\,\text{V}$, $U_\text{B} = 450\,\text{V}$, $P_\text{M} = 11.25\,\text{kW}$) results for the 2L-4S-BB converter, and $\eta = 98.9\%$ ($U_\text{F} = 640\,\text{V}$, $U_\text{B} = 720\,\text{V}$, $P_\text{M} = 11.25\,\text{kW}$) results for the 3L-8S-FC-BB converter. Further, the efficiency is also high in part-load operation, and values of $\eta < 97\%$ only result for a low power level of $1/4$ of the nominal power.

Last, **Fig. 12** compares the measured losses of the two systems against the calculated performance values for the mission profile operating points from **Fig. 4**, i.e., for climb ($U_\text{F} = 500\,\text{V}$ and $P_\text{M} = 14\,\text{kW}$) and cruise operation ($U_\text{F} = 620\,\text{V}$ and $P_\text{M} = 9\,\text{kW}$) and for the entire battery voltage range $U_\text{B} \in [450\,\text{V}, 720\,\text{V}]$. A close match between calculation and measurement is observed; furthermore, the calculated loss breakdown among the components is indicated. Thus, also the resulting mission profile efficiency values of 98.8% and 98.1% for the 2L-4S-BB and the 3L-8S-FC-BB converter, respectively, closely match the theoretical predictions from the optimization in **Sec. II**.
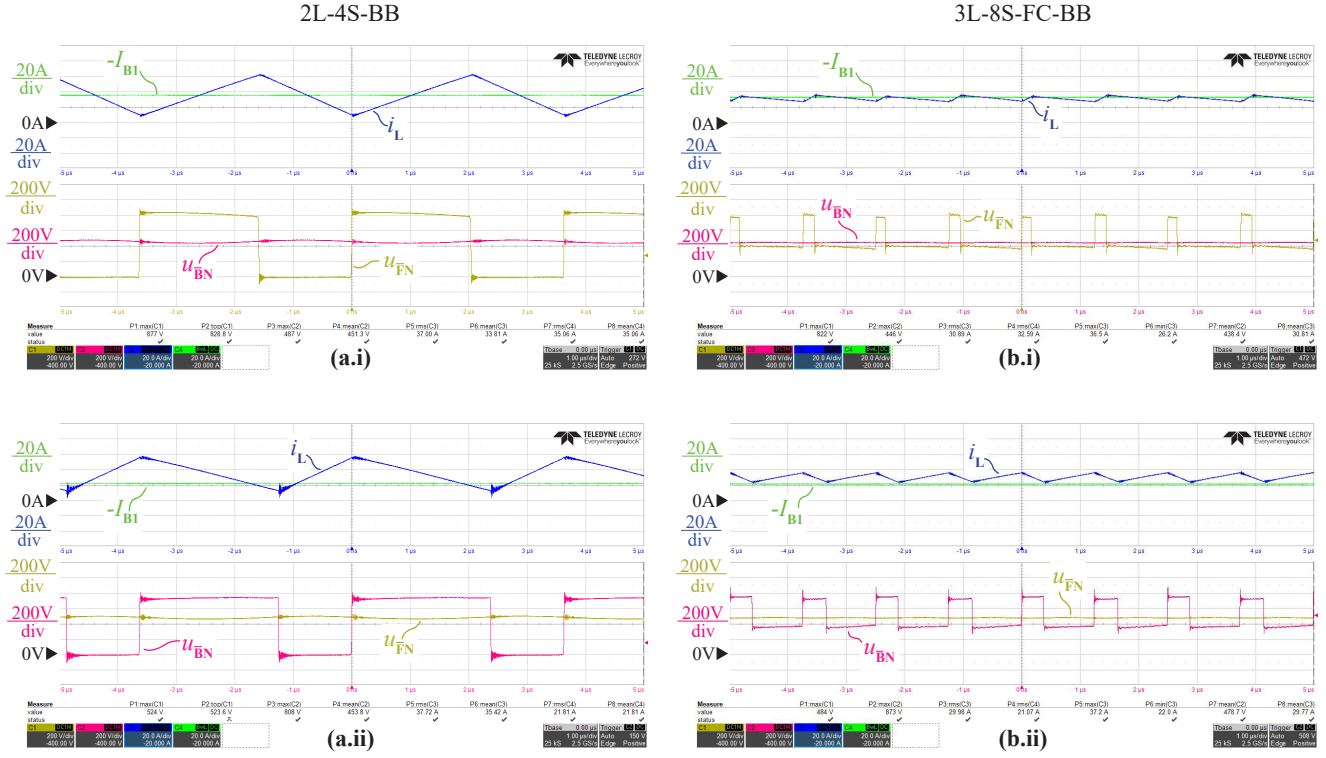
Fig. 10. Experimental nominal power ($P_{\mathrm{M}} = 15\,\mathrm{kW}$) waveforms of **(a)** the 2L-4S-BB (**Fig. 8a**), and **(b)** the 3L-8S-FC-BB (**Fig. 8b**) converter in **a.i,b.i** buck operation with an FC input voltage $U_{\mathrm{F}} = 800\,\mathrm{V}$ and a battery output voltage $U_{\mathrm{B}} = 450\,\mathrm{V}$, and **a.ii,b.ii** boost operation with an FC input voltage $U_{\mathrm{F}} = 480\,\mathrm{V}$ and a battery output voltage $U_{\mathrm{B}} = 720\,\mathrm{V}$. The displayed signals are the battery-side converter output current I_{B1}, the buck-boost inductor current i_{L}, as well as the buck-stage $u_{\bar{\mathrm{F}}\mathrm{N}}$ and boost-stage $u_{\bar{\mathrm{B}}\mathrm{N}}$ switch-node voltages. Note that due to the mutually exclusive operation of the buck and boost stage, the switch node is clamped to the respective positive dc-link terminal with $u_{\bar{\mathrm{B}}\mathrm{N}} = U_{\mathrm{B}}$ in buck and $u_{\bar{\mathrm{F}}\mathrm{N}} = U_{\mathrm{F}}$ in boost mode.
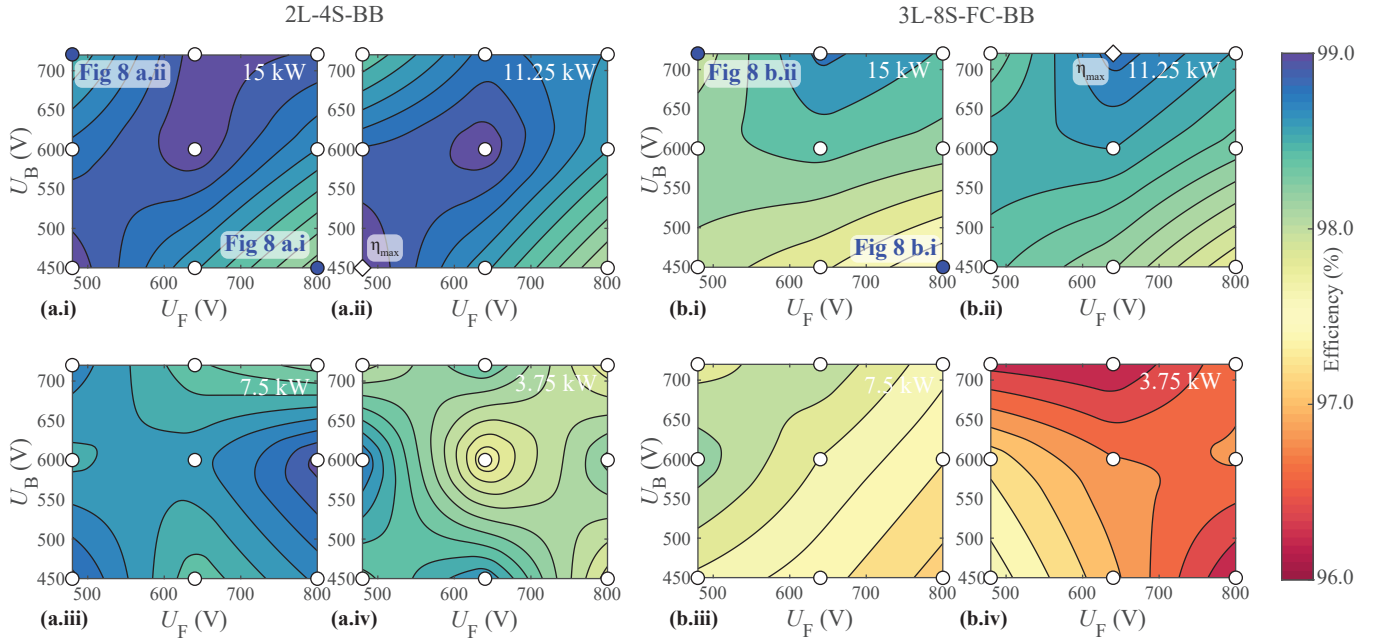
Fig. 11. Measured power conversion efficiency η as a function of the FC input U_{F} and battery output U_{B} voltage of **(a)** the 2L-4S-BB (**Fig. 8a**), and **(b)** the 3L-8S-FC-BB (**Fig. 8b**) converter for a module power level of **x.i** $P_{\mathrm{M}} = 15\,\mathrm{kW}$, **x.ii** $P_{\mathrm{M}} = 11.25\,\mathrm{kW}$, **x.iii** $P_{\mathrm{M}} = 7.5\,\mathrm{kW}$, and **x.iv** $P_{\mathrm{M}} = 3.75\,\mathrm{kW}$. The efficiency was recorded with a Norma D6100 power analyzer. The scatter points indicate the measured operating points and the loss map is generated using a triangulation-based natural neighbor interpolation. A peak efficiency $\eta_{\max} = 99.1\%$ ($U_{\mathrm{F}} = 480\,\mathrm{V}$, $U_{\mathrm{B}} = 450\,\mathrm{V}$, $P_{\mathrm{M}} = 11.25\,\mathrm{kW}$) and $\eta_{\max} = 98.9\%$ ($U_{\mathrm{F}} = 640\,\mathrm{V}$, $U_{\mathrm{B}} = 720\,\mathrm{V}$, $P_{\mathrm{M}} = 11.25\,\mathrm{kW}$) results for the 2L-4S-BB and 3L-8S-FC-BB converter, respectively, which is highlighted with a square scatter point. The two operating points considered in **Fig. 10** are further highlighted by dark scatter points in **(a.i)** and **(b.i)**.
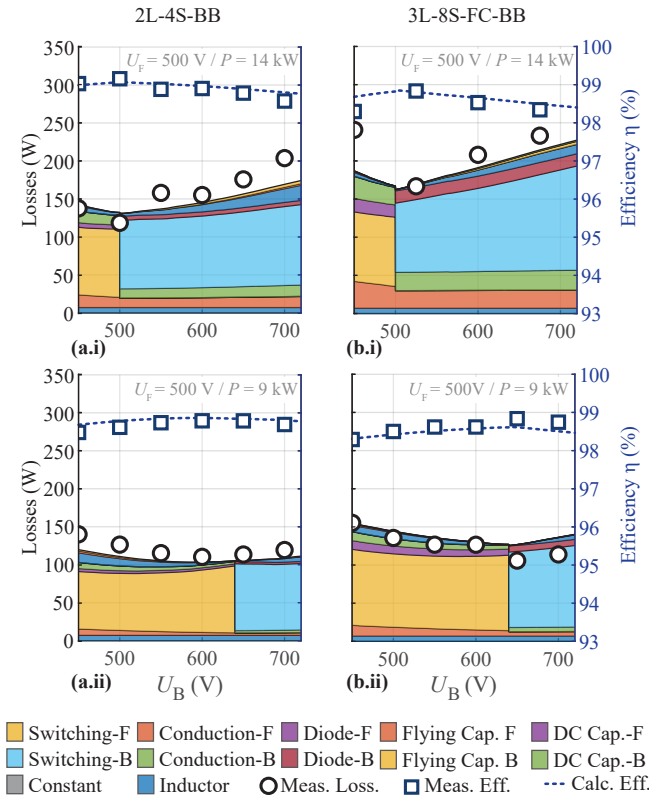
Fig. 12. Measured and calculated conversion losses and efficiency as a function of the battery output U_B voltag of **(a)** the 2L-4S-BB (**Fig. 8a**), and **(b)** the 3L-8S-FC-BB (**Fig. 8b**) converter for the relevant mission profile / drive cycle operating points, i.e., **x.i** $U_F = 500$ V and $P_M = 14$ kW (climb), and **x.ii** $U_F = 620$ V and $P_M = 9$ kW (cruise). The measured losses and efficiency values are highlighted by round and rectangular scatter points, respectively.

IV. CONCLUSION

The megatrend towards urbanization increases the interest in all-electric Vertical Takeoff and Landing (eVTOL) aircraft enabling simultaneously low operating space requirement for take-off and landing, and efficient cruising. There, hybrid Fuel-Cell (FC) / battery power supply architectures enable a substantial range increase for all-electric Vertical Takeoff and Landing (eVTOL) aircraft, however an ultra-lightweight Buck-Boost (BB) dc-dc converter is required to regulate the power flow between the two energy storages. Such BB converters are, however, understudied in literature and today limited to gravimetric power densities of 20 kW/kg, whereas a goal of 80 kW/kg is stated for 2040 [39].

This paper systematically identifies the optimal BB dc-dc converter realization among a set of topologies considering cutting edge component technology and the 3-Level 8-Switch BB (3L-8S-FC-BB) topology is found to be a sweet-spot concept between component stresses and system complexity and allows an optimal system realization with respect to maximum gravimetric power density at still competitive efficiencies. In contrast, due to the additional number of components, systems of higher complexity do not enable a further increase in gravimetric power density.

Two 15 kW prototypes with cutting edge wide-bandgap power semiconductor technology are built, a simple 2-Level 4-Switch BB (2L-4S-BB) converter with 44 kW/kg and a

3L-8S-FC-BB converter with 86 kW/kg, and extensively tested, where mission profile efficiency values above 98% result for both systems. Thus, the 3L-8S-FC-BB converter complies with the 2040 power density target and exceeds state-of-the-art BB converter systems by a factor of four with respect to weight.

Given this high performance of the BB converter, future research should in a first step address the remaining key power train components (mainly electric motors and inverter drives, as well as the battery and the FC which today remain inferior in terms of energy density compared to fossil fuels). Furthermore, another research project could address the scaling to higher power levels in the megawatt range as envisioned for future passenger jet liners. In this context, the question of whether a better performance could be achieved if a cryogenic cooling system was available could be investigated.

Last, safety is paramount in aviation and thus research towards more robust and fail-safe converter systems should be conducted with a special focus on the critical operating conditions which is of great importance for high-performance flying-capacitor multi-level converters [99].

APPENDIX A
DETAILS ON THE EVTOL MISSION PROFILE

The goal of the Appendix is to provide insights into the mission profile of the considered eVTOL aircraft in **Fig. 2**. First, the power and energy demand of the electric propulsion system for each phase of the mission profile in **Tab. III** is assessed by means of simplified aviation calculations (see, e.g., [100], [101]) and the estimated aircraft parameters in **Tab. IV**. Subsequently, the implications of the mission profile on the hybrid power supply architecture are discussed and an exemplary system dimensioning is provided. Last, the impact of the BB dc-dc converter efficiency and gravimetric power density on the entire power supply system is discussed in order to identify the sweet-spot converter metrics.

A. eVTOL Aircraft Drivetrain Power and Energy Demand

The aircraft mission (see **Fig. 2**) begins (and ends) with the propellers in hover configuration as illustrated in **Fig. 1a**. The power demand for each of the $N_R = 6$ tilt rotors in the flight phase 1 and 5 can be calculated as [19], [102]

$$P_P = \frac{m}{N_R \eta_{\text{hover}} \eta_D},\tag{1}$$

with m representing the aircraft mass, η_{hover} the hovering efficiency (expressed in kg of lift per kW of rotor power), and η_D the total efficiency of the electric motor and the integrated motor drive inverter. Note that tilt-rotor aircraft have a poor hovering efficiency η_{hover} compared to helicopters due to the high disk loading (i.e., a small rotor area relative to the aircraft mass) [100]–[103]: A typical eVTOL hovering efficiency of $\eta_{\text{hover}} = 5$ kg/kW is considered in **Tab. IV**; in contrast, helicopters achieve up to 15 kg/kW [102]. Thus, combined with the specified maximum take-off weight of $m = 1.9$ t and the total efficiency of the electric motor $\eta_D = 90\%$ (including the losses of the integrated motor drive inverter [20]), a total drive train power demand of $6 \cdot P_P = 420$ kW results during hovering (see **Fig. 13a**). When considering the technology from [20] (motor and integrated drive with

TABLE III
FLIGHT PHASES OF THE CONSIDERED eVTOL AIRCRAFT
MISSION PROFILE IN **FIG. 2**.

Phase	Mode	Duration	Height	Distance	Angle α
1	Hover	2 min	50 m	0 km	90.0°
2	Climb	5 min	1000 m	22 km	2.5°
3	Cruise	184 min	1000 m	766 km	0.0°
4	Descent	3 min	50 m	12 km	−4.5°
5	Hover	2 min	0 m	0 km	−90.0°

TABLE IV
MAIN SPECIFICATIONS OF THE HYBRID FC-BATTERY
POWERED eVTOL AIRCRAFT IN **FIG. 1**.

Component	Parameter	Value	Description
eVTOL	m	1900 kg	Take-off mass
	v	250 km/h	Cruise velocity
	N_R	6	Number of tilt rotors[1]
	L/D	12.5	Lift-to-drag ratio
	η_{hover}	5 kg/kW	Hovering efficiency
	η_R	85%	Rotor efficiency
	η_D	90%	Motor + drive efficiency
Battery Cell	e_B	340 Wh/kg	Gravim. energy density
	p_B	3.0 kW/kg	Gravim. power density (12C)
	η_B	60%	Efficiency (12C)[2]
Battery Pack	m_B	125 kg	Mass (incl. 0.8 derating)
	E_B	34 kWh	Nominal stored energy
	P_B	300 kW	Nominal power (12C)
Fuel Cell	p_F	2 kW/kg	Gravim. power density
	m_F	125 kg	Mass
	P_F	250 kW	Nominal power
	η_F	60%	Efficiency
H_2-Tank	GI	0.1	Gravim. index
	e_{H2}	33.3 kWh/kg	Gravim. energy density
	m_{H2}	30 kg	H_2 tank mass
	E_{H2}	1000 kWh	Nominal stored energy
	m_{tank}	300 kg	Mass (incl. H_2)

[1] $N_F = 2$ and $N_B = 4$ of the $N_R = 6$ tilt rotors are powered from the FC and the battery, respectively.
[2] Note that the low battery efficiency of $\eta_B = 60\%$ is a result of the high-C-rate operation (12C) during hovering with associated high current densities and associated capacity loss; E.g., for a lower discharge rate of 8C the efficiency increases substantially to approximately $\eta_B = 90\%$ [104].

12 kW/kg continuous power) the hovering power demand translates into a drive train weight of only 35 kg.

Upon reaching the minimally required height of 50 m in hovering mode, the aircraft tilts the rotors to transition into a more energy efficient fixed-wing cruising configuration which is maintained in the flight phases 2-4 [100], [101]. Here, the power demand for each of the $N_R = 6$ rotors can be calculated as [34]

$$P_P = \frac{mgv}{L/D + \sin(\alpha)}\frac{1}{N_R \eta_R \eta_D}, \qquad (2)$$

with the gravitation constant $g = 9.81\,\mathrm{m/s^2}$, the aircraft mass m, speed v, lift-to-drag-ratio L/D, and climb angle α, as well as the propeller efficiency η_R, and η_D denoting the overall efficiency of the electric motor and the integrated motor drive inverter and gearbox. Considering a typical $L/D = 12.5$ [100], [101], the total drive train power demand during climbing results to $6 \cdot P_P = 210\,\mathrm{kW}$ and then drops to $6 \cdot P_P = 135\,\mathrm{kW}$ for horizontal cruising ($\alpha = 0°$; see **Fig. 13**). In contrast, the negative climb angle α during descent can be selected such that the drag force is compensated

and the aircraft can glide with approximately zero drive power towards the target destination (alternatively, a part of the potential energy could be recuperated by selecting a more aggressive descent angle α). The subsequent hovering landing is modeled identical to the take-off and thus not listed in **Fig. 13a**.

The propulsion system energy demand during each phase of the mission profile results by multiplication of the propulsion system power $6 \cdot P_P$ with the respective duration (see **Tab. III**). In contrast to the maximum propulsion power demand ($6 \cdot P_P = 420\,\mathrm{kW}$ imposed by the hovering operation), the mission propulsion energy demand of $6 \cdot E_P = 460\,\mathrm{kWh}$ is dominated by the long cruise phase that contributes close to 90%.

### B. Hybrid Power Supply Architecture

The eVTOL aircraft power supply needs to be capable of providing both, the propulsion energy demand of $6 \cdot E_P = 460\,\mathrm{kWh}$ (plus a certain safety reserve) and the drive train peak power demand of $6 \cdot P_P = 420\,\mathrm{kW}$. The following section provides an example of a hybrid power supply architecture suitable for the considered mission profile.

Today's battery technology is limited to low gravimetric energy densities of approximately $200\,\mathrm{Wh/kg}$ to $300\,\mathrm{Wh/kg}$ [6], [8], [10], [11], [32]–[36] resulting in limited ranges compared to conventional aircraft [12], [25]. This weight penalty is further intensified by the fact that the weight of battery-powered aircraft does not decrease with flight time due to the absence of fuel consumption [35].

In contrast, H_2 features a gravimetric energy density of $e_{H2} = 33\,\mathrm{kWh/kg}$, thus outperforming kerosene with $12\,\mathrm{kWh/kg}$ by approximately a factor of three [10], [39]. Advantageously the refueling of the H_2 tank can be performed very rapidly. However, the required H_2 tanks are typically substantially more heavy than the encapsulated fuel itself: For example, 700 bar tanks feature gravimetric indices GI (i.e., the mass ratio of the fuel to the filled tank) of only up to 10% [39], [105], thus reducing the achievable effective gravimetric power density by an order of magnitude to $e_{H2} \cdot \mathrm{GI} = 3.3\,\mathrm{kWh/kg}$. Today, FCs with up to $2\,\mathrm{kW/kg}$ are available on a stack level, and the goal is to push the performance towards $10\,\mathrm{kW/kg}$ [106]. However, the limited gravimetric power density and the low response time of up to several seconds remain problematic [21], [38], [41]–[43].

A hybrid battery-FC power supply architecture [37]–[39] as highlighted in **Fig.1a,b** allows to leverage the specific advantages of the two energy carriers:

Advantageously, the high power demand of $6 \cdot P_P = 420\,\mathrm{kW}$ during hovering can be shared proportional to the number $N_F/N_R = 2/6$ and $N_B/N_R = 4/6$ of motors powered from the FC ($P_F = 140\,\mathrm{kW}$) and the battery ($P_B = 280\,\mathrm{kW}$), respectively, as highlighted in **Fig. 1b**. Thus, a relatively small battery can provide power boosting for the vertical take-off and landing such that the FC peak power requirement can be reduced [21] (see **Fig. 13a**). Here, cutting edge battery technology providing (on a cell level) a high gravimetric energy $e_B = 340\,\mathrm{Wh/kg}$ and power density $p_B = 3\,\mathrm{kW/kg}$ [104] is considered and the
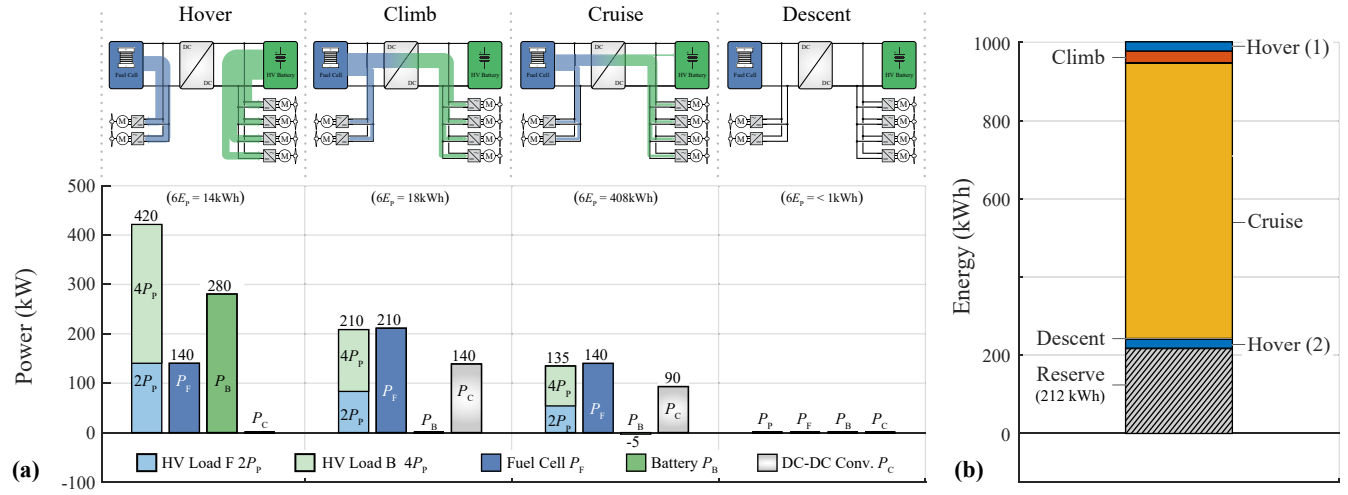
Fig. 13. Resulting eVTOL aircraft **(a)** power levels (and distribution) and **(b)** energy consumption in hover, climb, cruise and descent operation for the mission profile example in **Fig. 2** (details in **Tab. III**): The input power of the inverter drives $6 \cdot P_P$ is split between two propellers with $2 \cdot P_P$ which are attached to the FC bus U_F voltage and four propellers with $4 \cdot P_P$ which are attached to the battery bus U_B voltage. The BB dc-dc converter (power P_C) of the hybrid power supply architecture in **Fig. 1b** allows to adjust the power levels of the FC P_F and the battery P_B in the different phases of the aircraft mission such that the two energy storages can be used optimally.

power requirement $P_B = 280\,\text{kW}$ can be satisfied with a battery cell weight of $100\,\text{kg}$ ($E_B = 34\,\text{kWh}$) with sufficient margin. The battery pack weight thus results to $m_B = 125\,\text{kg}$ when considering a mass derating factor of 0.8 to account for the additional weight of the battery case and the battery management system. This high power density is enabled by extremely high discharging rates of up to 12C (and can be maintained even for low state-of-charge values) but comes at the cost of a relatively low efficiency which is estimated to $\eta_B = 60\%$ for the high-C-rate operation during hovering [104]. Thus, the battery is depleted by $16\,\text{kWh}$ (approximately 50%) during the two minute hovering interval, leaving sufficient margin in case of an emergency.

Subsequently, during the climb phase the aircraft power demand is fully covered by the FC: The interfacing BB dc-dc converter with an efficiency of $\eta_C = 98\%$ regulates a power flow $P_C = 4 \cdot P_P/\eta_C = 140\,\text{kW}$ from the FC to the battery side to cover the power demand of the $N_B = 4$ rotors. This results in a battery power $P_B = 0$, and an FC power $P_F = 2 \cdot P_P + 4 \cdot P_P/\eta_C = 210\,\text{kW}$, which also covers the conversion losses of the dc-dc converter. Note that this operating point requires the maximum FC power and the power-dependent FC voltage drops to its minimum value $U_F = 480\,\text{V}$. Considering a specific power of $p_F = 2\,\text{kW/kg}$ [107], [108] and a rated power of $P_F = 250\,\text{kW}$ (to provide a power safety margin), the weight of the FC results to $m_F = 125\,\text{kg}$.

Next, upon reaching cruise height, the propulsion power demand further decreases, and the BB dc-dc converter power reference of approximately $P_C = 90\,\text{kW}$ results in a slow battery recharge from the FC during this long phase of the mission profile, such that the full battery capacity is available again for the hovering during landing. Note that recharging can be performed at a slow rate with $\approx 0.2\text{C}$ such that the battery losses during this phase are extremely low compared to the hovering operation with 12C. Last, during

the descent towards the target destination, the system power demand reaches its minimum value (with a resulting power-dependent FC voltage $U_F = 800\,\text{V}$) followed again by a short high-power hovering interval during the final vertical landing phase of the mission.

For the dimensioning of the H_2 tank, the FC efficiency with a considered value of $\eta_F = 60\%$ has to be taken into account with $\frac{E_F}{\eta_F} = 770\,\text{kWh}$. To provide margin for an emergency, a tank capacity $E_{H2} = 1\,\text{MWh}$ is selected, which results with $e_{H2} \cdot \text{GI} = 3.3\,\text{kWh/kg}$ in a total (filled) tank weight of $300\,\text{kg}$. Hence, the entire FC power system (i.e., the FC and the associated H_2 tank) features a gravimetric energy density of $2350\,\text{Wh/kg}$ which is similar to the value of $2000\,\text{Wh/kg}$ described in [32].

C. Impact of the DC-DC Converter on the Hybrid Power Supply Weight

This section presents a highly simplified sensitivity analysis on the impact of the BB dc-dc converter on the entire power supply system weight. **Fig. 14** shows the overall Pareto front (i.e., envelope of the Pareto fronts of all considered topologies) of mission profile efficiency $\bar{\eta}$ vs. gravimetric power density γ of the BB dc-dc converters from **Fig. 7**. Each point on the Pareto front represents a converter design with a unique performance $(\bar{\eta}, \gamma)$ and the scatter color indicates the converter topology. As can be observed, the CF ZVS 2-Level 4-Switch BB (2L-4S-BB) topology is optimal for low values of γ up to $20\,\text{kW/kg}$, the Resonant Switched Capacitor 12-Switch BB (RSC-12S-BB) topology is optimal up to $60\,\text{kW/kg}$, and finally the 3-Level 8-Switch BB (3L-8S-FC-BB) enables $\gamma > 80\,\text{kW/kg}$.

With increasing gravimetric power density γ, the mass of the converter with $P_C = 150\,\text{kW}$ is decreasing with $m_C = P_C/\gamma$. Conversely, the hydrogen tank mass must be increased by Δm_{tank} to cover the additional conversion losses due to the decreasing mission profile efficiency. Here, the tank mass is scaled linearly with the conversion losses
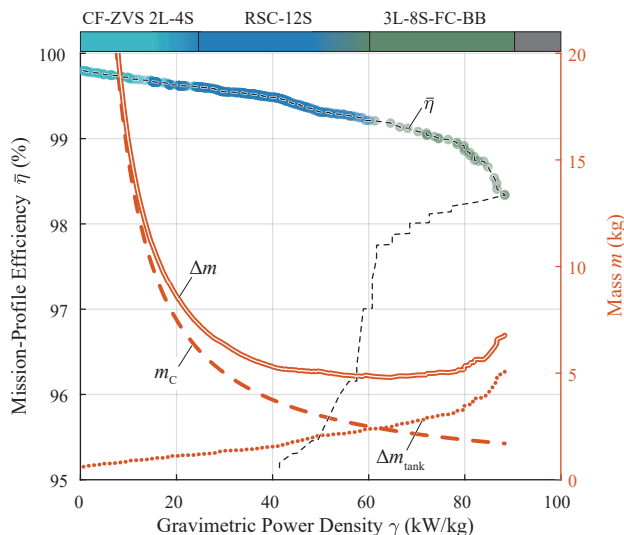
Fig. 14. Impact of the BB dc-dc converter on the total power supply weight: The overall Pareto front (i.e., envelope of the Pareto fronts of all considered topologies) of mission profile efficiency $\bar{\eta}$ vs. gravimetric power density γ is extracted from **Fig. 7**. With increasing gravimetric power density γ the mass m_C of the converter with $P_C = 150\,\text{kW}$ is decreasing. Conversely, the hydrogen tank mass must be increased by Δm_{tank} to cover the additional conversion losses due to the decreasing mission profile efficiency $\bar{\eta}$ with $\Delta m = m_C + \Delta m_{\text{tank}}$ representing the total change in power supply mass.

and is estimated as $\Delta m_{\text{tank}} = m_{\text{tank}}/\bar{\eta}$, i.e., with reference to the designed H$_2$ tank with $m_{\text{tank}} = 300\,\text{kg}$ and assuming a base-line scenario with $\bar{\eta} = 100\%$. Note that this calculation is highly simplified as for a given pressure level the tank wall thickness needs to remain constant: The resulting weight gains depend on the tank geometry (e.g., a cylinder or a sphere) and thus the increase of Δm_{tank} with decreasing $\bar{\eta}$ would be less steep in a more detailed analysis. The total change in power supply mass $\Delta m = m_C + \Delta m_{\text{tank}}$ is depicted in **Fig. 14** and a steep decrease can be observed up to gravimetric power density values up to $\gamma \approx 20\,\text{kW/kg}$ with a subsequent saturation and even a minor increase around $\gamma \approx 80\,\text{kW/kg}$, i.e., in contrast to purely battery powered aircraft [34], a high conversion efficiency is not the sole relevant performance factor when aiming at a low weight of the power supply system.

In absolute terms, it can be stated that the overall impact of the BB dc-dc converter remains minute with values of $\Delta m < 5\,\text{kg}$. Thus, also other crucial factors such as reliability, maintainability, environmental impact factors and cost should be considered in the design.

REFERENCES

[1] United Nations (UNO), Department of Economic and Social Affairs, "World urbanization prospects: The 2018 revision," 2019. [Online]. Available: https://www.un.org/development

[2] Uber Elevate, "Fast-forwarding to a future of on-demand urban air transportation," Oct. 2016. [Online]. Available: https://evtol.news/

[3] Joby Aviation, "US 2020/0148347 A1: Electric tiltrotor aircraft," Patent, 2020.

[4] M. Rimjha, S. Hotle, A. Trani, and N. Hinze, "Commuter demand estimation and feasibility assessment for urban air mobility in Northern California," *Transportation Research Part A: Policy and Practice*, vol. 148, pp. 506–524, Jun. 2021.

[5] M. Balac, R. L. Rothfeld, and S. Hörl, "The prospects of on-demand urban air mobility in Zurich, Switzerland," in *Proc. of the IEEE Intelligent Transportation Systems Conference (ITSC)*, Oct. 2019, pp. 906–913.

[6] K. Rajashekara, "Flying cars and e-VTOL vehicles: The future of transportation for reducing emissions," *EET&D MAGAZINE*, 2021.

[7] The Roland Berger Center for Smart Mobility, "Urban air mobility," 2020. [Online]. Available: https://www.rolandberger.com/publications/

[8] X.-G. Yang, T. Liu, S. Ge, E. Rountree, and C.-Y. Wang, "Challenges and key requirements of batteries for electric vertical takeoff and landing aircraft," *Joule*, vol. 5, no. 7, pp. 1644–1659, Jul. 2021.

[9] A. M. Stoll, J. B. Bevirt, P. P. Pei, and E. V. Stilson, "Conceptual design of the Joby S2 electric VTOL PAV," *Proc. of the AIAA Aviation Technology, Integration, and Operations Conference*, pp. 16–20, Jun. 2014.

[10] N. Swaminathan, S. R. P. Reddy, K. Rajashekara, and K. S. Haran, "Flying cars and eVTOLs—Technology advancements, powertrain architectures, and design," *IEEE Transactions on Transportation Electrification*, vol. 8, no. 4, pp. 4105–4117, Dec. 2022.

[11] O. Ugwueze, T. Statheros, N. Horri, M. A. Bromfield, and J. Simo, "An efficient and robust sizing method for eVTOL aircraft configurations in conceptual design," *Aerospace*, vol. 10, no. 3, p. 311, Mar. 2023. [Online]. Available: https://www.mdpi.com/2226-4310/10/3/311

[12] M. Hepperle, "NATO STO-MP-AVT-209: Electric flight – Potential and limitations," 2012. [Online]. Available: https://elib.dlr.de/78726/1/MP-AVT-209-09.pdf

[13] J. Ebersberger, M. Hagedorn, M. Lorenz, and A. Mertens, "Potentials and comparison of inverter topologies for future all-electric aircraft propulsion," *IEEE Journal of Emerging and Selected Topics in Power Electronics*, vol. 10, no. 5, pp. 5264–5279, Oct. 2022.

[14] H. H. Sathler, T. Zhao, F. Costa, B. Cougo, G. Segond, R. Burgos, and D. Labrousse, "Design of three-level flying-capacitor commutation cells with four paralleled 650 V/60 A GaN HEMTs," *Proc. of the IEEE Applied Power Electronics Conference and Exposition (APEC)*, pp. 2277–2284, Mar. 2021.

[15] H. H. Sathler, "Optimization of GaN-based series-parallel multilevel three-phase inverter for aircraft applications," Ph.D. dissertation, Université Paris-Saclay, 2022.

[16] F. F. Wang, R. Chen, and Z. Dong, "Power electronics: A critical enabler of future hydrogen–electric systems for aviation," *IEEE Electrification Magazine*, vol. 10, no. 2, pp. 57–68, Jun. 2022.

[17] S. Sripad and V. Viswanathan, "The promise of energy-efficient battery-powered urban aircraft," *Proceedings of the National Academy of Sciences*, vol. 118, no. 45, pp. 1–3, Nov. 2021.

[18] N. André and M. Hajek, "Robust environmental life cycle assessment of electric VTOL concepts for urban air mobility," in *Proc. of the AIAA Aviation Forum*. Dallas (TX): American Institute of Aeronautics and Astronautics, Jun. 2019.

[19] A. Kasliwal, N. J. Furbush, J. H. Gawron, J. R. McBride, T. J. Wallington, R. D. De Kleine, H. C. Kim, and G. A. Keoleian, "Role of flying cars in sustainable mobility," *Nature Communications*, vol. 10, no. 1, p. 1555, Apr. 2019.

[20] H3X, "HPDM-250 (datasheet v 1.9)." [Online]. Available: https://www.h3x.tech/

[21] J. M. Collins and D. McLarty, "All-electric commercial aviation with solid oxide fuel cell-gas turbine-battery hybrids," *Applied Energy*, vol. 265, p. 114787, May 2020.

[22] X. Zhang, C. L. Bowman, T. C. O'Connell, and K. S. Haran, "Large electric machines for aircraft electric propulsion," *IET Electric Power Applications*, vol. 12, no. 6, pp. 767–779, 2018.

[23] J. D. Nicholas, "Highlights from the 2013 national science foundation solid oxide fuel cell promise, progress, and priorities (SOFC-PPP) workshop," *Interface Magazine*, vol. 22, no. 4, pp. 49–54, Jan. 2013.

[24] J. J. Scheidler, "Preliminary design of the superconducting rotor for NASA's 1.4 MW high-efficiency electric machine," in *Proc. of the AIAA Joint Propulsion Conference*. Cincinnati (OH): American Institute of Aeronautics and Astronautics, Jul. 2018.

[25] P. Wheeler, T. S. Sirimanna, S. Bozhko, and K. S. Haran, "Electric/hybrid-electric aircraft propulsion systems," *Proceedings of the IEEE*, vol. 109, no. 6, pp. 1115–1127, Jun. 2021.

[26] J. Benzaquen, J. He, and B. Mirafzal, "Toward more electric powertrains in aircraft: Technical challenges and advancements," *CES Transactions on Electrical Machines and Systems*, vol. 5, no. 3, pp. 177–193, Sep. 2021.

[27] R. Sugouchi, M. Komiya, S. Miura, M. Iwakuma, K. Yoshida, T. Sasayama, T. Yoshida, K. Yamamoto, Y. Sasamori, H. Honda, Y. Hase, M. Shuto, M. Konno, and T. Izumi, "Conceptual design and electromagnetic analysis of 2 MW fully superconducting synchronous motors with superconducting magnetic shields for turbo-electric propulsion system," *IEEE Transactions on Applied Superconductivity*, vol. 30, no. 4, pp. 1–5, Jun. 2020.

[28] K. Yamaguchi, K. Katsura, T. Yamada, and Y. Sato, "High power density SiC-based inverter with a power density of 70kW/liter or 50kW/kg," *IEEJ Journal of Industry Applications*, vol. 8, no. 4, pp. 694–703, Jul. 2019.

[29] D. Cittanti, E. Vico, E. Armando, and R. Bojoi, "Analysis and conceptualization of a 400V 100 kVA full-GaN double bridge inverter for next-generation electric vehicle drives," in *Proc. of the IEEE Transportation Electrification Conference & Expo (ITEC)*, Jun. 2022, pp. 740–747.

[30] D. Cittanti, F. Stella, E. Vico, C. Liu, J. Shen, G. Xiu, and R. Bojoi, "Analysis, design and experimental assessment of a high power density ceramic DC-link capacitor for a 800 V 550 kVA electric vehicle drive inverter," *IEEE Transactions on Industry Applications*, pp. 1–13, 2023.

[31] M. Meindl, J. Zettelmeier, C. Bentheimer, F. Hilpert, and M. März, "Aircraft drive inverter design at physical limits," in *Proc. of the IEEE Workshop on Power Electronics for Aerospace Applications (PEASA)*, Jul. 2023, pp. 1–6.

[32] E. Okumus, F. G. Boyaci San, O. Okur, B. E. Turk, E. Cengelci, M. Kilic, C. Karadag, M. Cavdar, A. Turkmen, and M. S. Yazici, "Development of boron-based hydrogen and fuel cell system for small unmanned aerial vehicle," *International Journal of Hydrogen Energy*, vol. 42, no. 4, pp. 2691–2697, 2017.

[33] T. Bærheim, J. J. Lamb, J. K. Nøland, and O. S. Burheim, "Potential and limitations of battery-powered all-electric regional flights—A Norwegian case study," *IEEE Transactions on Transportation Electrification*, vol. 9, no. 1, pp. 1809–1825, Mar. 2023.

[34] J. Ebersberger, L. Fauth, R. Keuter, Y. Cao, Y. Freund, R. Hanke-Rauschenbach, B. Ponick, A. Mertens, and J. Friebe, "Power distribution and propulsion system for an all-electric short-range commuter aircraft—A case study," *IEEE Access*, vol. 10, pp. 114 514–114 539, 2022.

[35] I. Staack, A. Sobron, and P. Krus, "The potential of full-electric aircraft for civil transportation: from the Breguet range equation to operational aspects," *CEAS Aeronautical Journal*, vol. 12, no. 4, pp. 803–819, Nov. 2021.

[36] A. Misley, M. D'Arpino, P. Ramesh, and M. Canova, "A real-time energy management strategy for hybrid electric aircraft propulsion systems," in *Proc. of the AIAA/IEEE Electric Aircraft Technologies Symposium (EATS)*, Aug. 2021, pp. 1–11.

[37] J. A. Oliver, P. Zumel, M. Sanz, C. Raga, D. Izquierdo, O. Garcia, A. Barrado, R. Prieto, R. Azcona, B. Delicado, and J. A. Cobos, "High level decision methodology for the selection of a fuel cell based power distribution architecture for an aircraft application," *Proc. of the IEEE Energy Conversion Congress and Exposition (ECCE USA)*, no. 1, pp. 459–464, Sep. 2009.

[38] J. Y. Kim, B. S. Lee, Y. J. Lee, and J. K. Kim, "Integrated multi mode converter with single inductor for fuel cell electric vehicles," *IEEE Transactions on Industrial Electronics*, vol. 69, no. 11, pp. 11 001–11 011, 2022.

[39] M. Schmelcher, J. Häßy, and M. Schmelcher, "Hydrogen fuel cells for aviation?" in *Proc. of the International Society for Air Breathing Engines (ISABE)*, 2022.

[40] F. Mazzeo and G. Di Ilio, "Fuel cell hybrid electric propulsion system for a lightweight helicopter: Design and performance analysis in urban air mobility scenario," *International Journal of Hydrogen Energy*, Oct. 2023.

[41] D. Ciliberti, P. Della Vecchia, V. Memmolo, F. Nicolosi, G. Wortmann, and F. Ricci, "The enabling technologies for a quasi-zero emissions commuter aircraft," *Aerospace*, vol. 9, no. 6, p. 319, Jun. 2022.

[42] P. J. Smith, W. R. Bennett, I. J. Jakupca, R. P. Gilligan, and L. G. Edwards, "NASA/TM-20210018094: Proton exchange membrane fuel cell tansient load response," 2021. [Online]. Available: https://history.nasa.gov

[43] P. Pei, X. Yuan, J. Gou, and P. Li, "Dynamic response during PEM fuel cell loading-up," *MDPI Materials*, vol. 2, no. 3, pp. 734–748, Jul. 2009.

[44] S. Coday, N. Ellis, N. Stokowski, and R. Pilawa-Podgurski, "Design and implementation of a (flying) flying capacitor multilevel converter," in *Proc. of the IEEE Applied Power Electronics Conference and Exposition (APEC)*, Mar. 2022, pp. 542–547.

[45] S. Coday, N. M. Ellis, N. Stokowski, and R. C. Pilawa-Podgurski, "Design and flight qualification of a flying capacitor multilevel converter for electric aircraft applications," *IEEE Transactions on Transportation Electrification*, pp. 1–1, 2023.

[46] Fraunhofer Institute for Integrated Systems and Device Technology (IISB), "Bidirectional full SiC 200 kW DC-DC converter for electric, hybrid and fuel cell vehicles," 2015. [Online]. Available: https://www.iisb.fraunhofer.de

[47] G. Calderon-Lopez, J. Scoltock, Y. Wang, I. Laird, X. Yuan, and A. J. Forsyth, "Power-dense bi-directional DC–DC converters with high-performance inductors," *IEEE Transactions on Vehicular Technology*, vol. 68, no. 12, pp. 11 439–11 448, Dec. 2019.

[48] M. Warncke, S. Fahlbusch, and K. F. Hoffmann, "DC/DC-converter for fuel cell integration in more electric aircraft applications," in *Proc. of the European Conference on Power Electronics and Applications (EPE-ECCE Europe)*, Sep. 2017, pp. P.1–P.10.

[49] G.-J. Su, C. White, and Z. Liang, "Design and evaluation of a 6.6 kW GaN converter for onboard charger applications," in *Proc. of the IEEE Workshop on Control and Modeling for Power Electronics (COMPEL)*, Jul. 2017, pp. 1–6.

[50] BrightLoop, "Buck-boost DC-DC HV-HV converter." [Online]. Available: https://brightloop.fr/en/product-category/dcdc-hv-hv/

[51] C. Gammeter, F. Krismer, and J. W. Kolar, "Comprehensive conceptualization, design, and experimental verification of a weight-optimized all-SiC 2 kV/700 V DAB for an airborne wind turbine," *IEEE Journal of Emerging and Selected Topics in Power Electronics*, vol. 4, no. 2, pp. 638–656, Jun. 2016.

[52] D. Menzi, Z. Yu, J. Huber, and J. W. Kolar, "Comparative evaluation of ultra-lightweight buck-boost DC-DC converter topologies for future eVTOL aircraft," in *Proc. of the IEEE Workshop on Control and Modeling for Power Electronics (COMPEL)*, 2022.

[53] D. Maksimović, "Machine learning estimators for power electronics design and optimization," Oct. 2021, presentation at the ECPE Workshop on Steps towards Design Automation & Artificial Intelligence in Power Electronics.

[54] D. Maksimovic, "SiC-based high-density composite electric drive-train converters," May 2022, presentation at the IEEE PELS San Francisco Bay Area Chapter Seminar.

[55] S. Coday, A. Barchowsky, and R. C. Pilawa-Podgurski, "A 10-level GaN-based Flying Capacitor Multilevel Boost Converter for Radiation-Hardened Operation in Space Applications," in *Proc. of the IEEE Applied Power Electronics Conference and Exposition (APEC)*, Jun. 2021, pp. 2798–2803, iSSN: 2470-6647 Coday10levelFCSpaceApplications2021.

[56] S. Coday, N. Ellis, Z. Liao, and R. C. N. Pilawa-Podgurski, "A lightweight multilevel power converter for electric aircraft drive-train," in *Proc. of the IEEE Energy Conversion Congress and Exposition (ECCE USA)*, 2021, pp. 1507–1513.

[57] H. Kim, H. Chen, D. Maksimovic, R. Erickson, Z. Cole, B. Passmore, and K. Olejniczak, "SiC-MOSFET composite boost converter with 22 kW/L power density for electric vehicle application," in *Proc. of the IEEE Applied Power Electronics Conference and Exposition (APEC)*, Tampa (FL), Mar. 2017, pp. 134–141.

[58] G. Calderon-Lopez and A. J. Forsyth, "High power density DC-DC converter with SiC MOSFETs for electric vehicles," in *Proc. of the IET International Conference on Power Electronics, Machines and Drives (PEMD)*, Apr. 2014, pp. 1–6.

[59] A. H. Wienhausen, A. Sewergin, and R. W. De Doncker, "Highly integrated two-phase SiC boost converter with 3D-printed fluid coolers and 3D-printed inductor bobbins," in *Proc. of the Power Conversion and Intelligent Motion Conference (PCIM)*, 2018, pp. 317–324.

[60] A. H. Wienhausen, "High integration of power electronic converters enabled by 3D printing," Ph.D. dissertation, RWTH Aachen, 2019.

[61] A. H. Wienhausen, A. Sewergin, and R. W. De Doncker, "Ultra-high power density full-SiC boost converter enabled by advanced 3D-printing techniques," in *Proc. of the IEEE Applied Power Electronics Conference and Exposition (APEC)*, Anaheim (CA), Mar. 2019, pp. 1281–1288.

[62] ——, "Highly integrated boost converter featuring a power density of 98 kW/dm^3 and 56 kW/kg," in *Proc. of the International Exhibition and Conference for Power Electronics, Intelligent Motion, Renewable Energy and Energy Management (PCIM Europe digital days)*, Jul. 2020, pp. 1–5.

[63] T.-R. Granados-Luna, I. Araujo-Vargas, A. J. Forsyth, K. Cano-Pulido, P.-E. Velázquez-Elizondo, I. Cervantes, F. Gómez-Olguín, and A. Villarruel-Parra, "Two-phase, dual interleaved buck–boost DC–DC converter for automotive applications," *IEEE Transactions on Industry Applications*, vol. 56, no. 1, pp. 390–402, Jan. 2020.

[64] F. Gómez-Olguín, I. Araujo-Vargas, T. Granados-Luna, P. Velázquez-Elizondo, K. Cano-Pulido, and A. Villarruel-Parra, "Design and assessment of a 30 kW/75 kHz DC-DC, two-phase dual interleaved buck-boost converter," in *Proc. of the IEEE Texas Power and Energy Conference (TPEC)*, Feb. 2018, pp. 1–6.

[65] X.-F. Cheng, Z. Peng, Y. Yang, Z. Liang, C. Wu, Z. Shao, and D. Wang, "A 5.6 kW 11.7 kW per kg four-phase interleaved buck converter for the unmanned aerial vehicle," *Journal of Electrical Engineering & Technology*, vol. 17, no. 2, pp. 1077–1086, Mar. 2022.

[66] Z. Zhang, H. Tu, X. She, T. Sadilek, R. Ramabhadran, H. Hu, and W. Earls, "High-efficiency silicon carbide-based buck-boost converter in an energy storage system: Minimizing complexity and maximizing efficiency," *IEEE Industry Applications Magazine*, vol. 27, no. 3, pp. 51–62, 2021.

[67] X. Ren, Z. Tang, X. Ruan, J. Wei, and G. Hua, "Four switch buck-boost converter for telecom DC-DC power supply applications," in *Proc. of the IEEE Applied Power Electronics Conference and Exposition (APEC)*, Feb. 2008, pp. 1527–1530.

[68] X. Li, Y. Liu, and Y. Xue, "Four-switch buck–boost converter based on model predictive control with smooth mode tansition capability," *IEEE Transactions on Industrial Electronics*, vol. 68, no. 10, pp. 9058–9069, Oct. 2021.

[69] W. Wu and F. Blaabjerg, "Aalborg inverter - A new type of 'buck in buck, boost in boost' grid-tied inverter," *Proc. of the IEEE Applied Power Electronics Conference and Exposition (APEC)*, pp. 460–467, May 2013.

[70] S. Waffler and J. W. Kolar, "A novel low-loss modulation strategy for high-power bidirectional buck + boost converters," *IEEE Transactions on Power Electronics*, vol. 24, no. 6, pp. 1589–1599, 2009.

[71] Z. Zhou, H. Li, and X. Wu, "A constant frequency ZVS control system for the four-switch buck–boost DC–DC converter with reduced inductor current," *IEEE Transactions on Power Electronics*, vol. 34, no. 7, pp. 5996–6003, Jul. 2019.

[72] T. Meynard and H. Foch, "Multi-level choppers for high voltage applications," *European Power Electronics Journal (EPE)*, vol. 2, no. 1, pp. 45–50, 1992.

[73] T. A. Meynard, "Modeling of multilevel converters," *IEEE Transactions on Industrial Electronics*, vol. 44, no. 3, pp. 356–364, 1997.

[74] Y. Lei, C. Barth, S. Qin, W. C. Liu, I. Moon, A. Stillwell, D. Chou, T. Foulkes, Z. Ye, Z. Liao, and R. C. Pilawa-Podgurski, "A 2-kW single-phase seven-level flying capacitor multilevel inverter with an active energy buffer," *IEEE Transactions on Power Electronics*, vol. 32, no. 11, pp. 8570–8581, 2017.

[75] J. Azurza Anderson, G. Zulauf, J. W. Kolar, and G. Deboy, "New figure-of-merit combining semiconductor and multi-level converter properties," *IEEE Open Journal of Power Electronics*, vol. 1, no. July, pp. 322–338, 2020.

[76] S. Qin, Y. Lei, C. Barth, W. C. Liu, and R. C. Pilawa-Podgurski, "A high power density series-stacked energy buffer for power pulsation decoupling in single-phase converters," *IEEE Transactions on Power Electronics*, vol. 32, no. 6, pp. 4905–4924, 2017.

[77] Z. Ye, Y. Lei, Z. Liao, and R. C. Pilawa-Podgurski, "Investigation of capacitor voltage balancing in practical implementations of flying capacitor multilevel converters," in *Proc. of the Workshop on Control and Modeling for Power Electronics (COMPEL)*, 2017.

[78] E. Hnatek, *Design of solid-state power supplies*. Van Nostrand Reinhold Company, 1971.

[79] R. M. Button, "NASA/TM—1998-206628: A modular PMAD system for small spacecraft," 1998. [Online]. Available: https://history.nasa.gov

[80] H. Chen, H. Kim, R. Erickson, and D. Maksimovic, "Electrified automotive powertrain architecture using composite DC-DC converters," *IEEE Transactions on Power Electronics*, vol. 32, no. 1, pp. 98–116, 2017.

[81] M. C. Fernandez, A. Ghosh, and R. W. Erickson, "Drive cycle based multi-objective optimization of 50 kW SiC composite DC-DC converter design for electrified automotive applications," in *Proc. of the Workshop on Wide Bandgap Power Devices and Applications (WiPDA)*, Oct. 2019, pp. 164–170.

[82] B. Stevanovic, G. S. Salinas, P. Alou Cervera, J. A. Cobos, and M. Vasic, "Comparative evaluation of the two multi-level concepts with full ZVS operation employing WBG devices for use in 1500-V PV systems," *IEEE Transactions on Industry Applications*, vol. 9994, no. c, pp. 1–1, 2022.

[83] M. Vasic, D. Serrano, P. Alou, J. A. Oliver, P. Grbovic, and J. A. Cobos, "Comparative analysis of two compact and highly efficient resonant switched capacitor converters," in *Proc. of the IEEE Applied Power Electronics Conference and Exposition (APEC)*, Mar. 2018, pp. 2168–2174.

[84] H. N. Tran, T. T. Le, H. Jeong, S. Kim, and S. Choi, "A 300 kHz, 63 kW/L ZVT DC-DC converter for 800-V fuel cell electric vehicles," *IEEE Transactions on Power Electronics*, vol. 37, no. 3, pp. 2993–3006, 2022.

[85] M. Antivachis, D. Bortis, L. Schrittwieser, and J. W. Kolar, "Three-phase buck-boost Y-inverter with wide DC input voltage range," in *Proc. of the IEEE Applied Power Electronics Conference and Exposition (APEC)*, 2018, pp. 1492–1499.

[86] M. Baumann and J. Kolar, "A novel control concept for reliable operation of a three-phase three-switch buck-type unity-power-factor rectifier with integrated boost output stage under heavily unbalanced mains condition," *IEEE Transactions on Industrial Electronics*, vol. 52, no. 2, pp. 399–409, Apr. 2005.

[87] J. Celikovic, P. Cavallini, S. Abedinpour, and D. Maksimovic, "Minimum-deviation transient response in non-inverting buck-boost DC-DC converters," in *Proc. of the IEEE Workshop on Control and Modeling for Power Electronics (COMPEL)*, 2020.

[88] T. Urkin and M. M. Peretz, "Digital CPM controller for a non-inverting buck–boost converter with unified hardware for steady-state and optimized transient conditions," *IEEE Transactions on Power Electronics*, vol. 35, no. 8, pp. 8794–8804, Aug. 2020.

[89] J. W. Kolar, U. Drofenik, J. Biela, M. L. Heldwein, H. Ertl, T. Friedli, and S. D. Round, "PWM converter power density barriers," in *Proc. of the IEEE Power Conversion Conference (PCC)*, Apr. 2007.

[90] P. Papamanolis, T. Guillod, F. Krismer, and J. W. Kolar, "Minimum loss operation and optimal design of high-frequency inductors for defined core and litz wire," *IEEE Open Journal of Power Electronics*, vol. 1, no. October, pp. 469–487, 2020.

[91] TDK, "Product Brief CeraLink Capacitors," 2019. [Online]. Available: www.tdk-electronics.tdk.com

[92] L. Hoffmann, C. Gautier, S. Lefebvre, and F. Costa, "Optimization of the driver of GaN power transistors through measurement of their thermal behavior," *IEEE Transactions on Power Electronics*, vol. 29, no. 5, pp. 2359–2366, 2014.

[93] D. Zhang, M. Guacci, M. Haider, D. Bortis, J. W. Kolar, and J. Everts, "Three-phase bidirectional buck-boost current DC-link EV battery charger featuring a wide output voltage range of 200 to 1000V," in *Proc. of the IEEE Energy Conversion Congress and Exhibition (ECCE USA)*, Oct. 2020, pp. 4555–4562.

[94] M. Guacci, J. Azurza Anderson, K. L. Pally, D. Bortis, J. W. Kolar, M. J. Kasper, J. Sanchez, and G. Deboy, "Experimental characterization of silicon and gallium nitride 200 V power semiconductors for modular/multi-level converters using advanced measurement techniques," *IEEE Journal of Emerging and Selected Topics in Power Electronics*, vol. 8, no. 3, pp. 2238–2254, 2020.

[95] S. Coday, C. B. Barth, and R. C. Pilawa-Podgurski, "Characterization and modeling of ceramic capacitor losses under large signal operating conditions," in *Proc. of the IEEE Workshop on Control and Modeling for Power Electronics (COMPEL)*, 2018, pp. 1–8.

[96] D. Han, J. Noppakunkajorn, and B. Sarlioglu, "Comprehensive efficiency, weight, and volume comparison of SiC- and Si-based bidirectional DC–DC converters for hybrid electric vehicles," *IEEE Transactions on Vehicular Technology*, vol. 63, no. 7, pp. 3001–3010, Sep. 2014.

[97] C. R. Sullivan, B. A. Reese, A. L. Stein, and P. A. Kyaw, "On size and magnetics: Why small efficient power inductors are rare," in *Proc. of the IEEE International Symposium on 3D Power Electronics Integration and Manufacturing (3DPEIM)*, 2016.

[98] M. Khazraei, H. Sepahvand, K. A. Corzine, and M. Ferdowsi, "Active capacitor voltage balancing in single-phase flying-capacitor multilevel power converters," *IEEE Transactions on Industrial Electronics*, vol. 59, no. 2, pp. 769–778, 2012.

[99] S. Coday, N. M. Ellis, and R. C. Pilawa-Podgurski, "Modeling and analysis of shutdown dynamics in flying capacitor multilevel converters," *IEEE Transactions on Power Electronics*, pp. 1–12, 2023. [Online]. Available: https://ieeexplore.ieee.org/abstract/document/10159129

[100] P. S. Moller, "Performance evaluation of select personal air vehicles," 2020.

[101] A. Jha, N. Prabhakar, D. Karbowski, and B. German, "Urban air mobility: A preliminary case study for Chicago and Atlanta," in *Proc. of the IEEE Transportation Electrification Conference & Expo (ITEC)*, Jun. 2022, pp. 300–306.

[102] M. D. Maisel, D. J. Giulianetti, and D. C. Dugan, "NASA SP-2000-4517: The history of the XV-15 tilt rotor research aircraft." [Online]. Available: https://history.nasa.gov

[103] J. M. Wang, C. T. Jones, and M. W. Nixon, "A variable diameter short haul civil tiltrotor," in *Proc. of the Annual Forum of the American Helicoper Society*, vol. 55, May 1999.

[104] Ionblox, "High Energy AV Cell," 2023. [Online]. Available: https://www.ionblox.com/air

[105] J. Mukhopadhaya and D. Rutherford, "White paper: Performance analysis of evolutionary hydrogen-powered aircraft," Jan. 2022. [Online]. Available: www.theicct.org

[106] International Air Transport Association, "Aircraft technology net zero roadmap," 2023. [Online]. Available: https://www.iata.org/contentassets

[107] H. Yumiya, M. Kizaki, and H. Asai, "Toyota Fuel Cell System (TFCS)," *MDPI World Electric Vehicle Journal*, vol. 7, no. 1, pp. 85–92, Mar. 2015. [Online]. Available: https://www.mdpi.com/2032-6653/7/1/85

[108] HyPoint, "Technical white paper," Nov. 2021. [Online]. Available: https://hypoint.com/